

Euclid preparation

Impact of galaxy intrinsic alignment modelling choices on *Euclid* 3 × 2 pt cosmology

Euclid Collaboration: D. Navarro-Gironés^{★1}, I. Tutzus^{2,3,4}, M. Crocce^{2,3}, S. Gouyou Beauchamps^{3,2}, R. Paviot⁵, B. Joachimi⁶, J. Ruiz-Zapatero⁶, D. Sciotti^{7,8}, N. Tessore⁹, G. Cañas-Herrera^{10,1}, P. Carrilho¹¹, J. M. Coloma-Nadal², H. Hoekstra¹, A. Porredon¹², B. Altieri¹³, S. Andreon¹⁴, C. Baccigalupi^{15,16,17,18}, M. Baldi^{19,20,21}, S. Bardelli²⁰, A. Biviano^{16,15}, E. Branchini^{22,23,14}, M. Brescia^{24,25}, S. Camera^{26,27,28}, V. Capobianco²⁸, C. Carbone²⁹, V. F. Cardone^{7,8}, J. Carretero^{12,30}, F. J. Castander^{2,3}, M. Castellano⁷, G. Castignani²⁰, S. Cavuoti^{25,31}, K. C. Chambers³², C. Colodro-Conde³³, G. Congedo¹⁰, C. J. Conselice³⁴, L. Conversi^{35,13}, Y. Copin³⁶, F. Courbin^{37,38,39}, H. M. Courtois⁴⁰, A. Da Silva^{41,42}, H. Degaudenzi⁴³, G. De Lucia¹⁶, H. Dole⁴⁴, F. Dubath⁴³, C. A. J. Duncan¹⁰, X. Dupac¹³, S. Escoffier⁴⁵, M. Farina⁴⁶, R. Farinelli²⁰, S. Farrens⁵, S. Ferriol³⁶, F. Finelli^{20,47}, P. Fosalba^{3,2}, S. Fotopoulou⁴⁸, N. Fourmanoit⁴⁵, M. Frailis¹⁶, E. Franceschi²⁰, M. Fumana²⁹, S. Galeotta¹⁶, K. George⁴⁹, B. Gillis¹⁰, C. Giocoli^{20,21}, J. Gracia-Carpio⁵⁰, A. Grazian⁵¹, F. Grupp^{50,52}, S. V. H. Haugan⁵³, W. Holmes⁵⁴, F. Hormuth⁵⁵, A. Hornstrup^{56,57}, K. Jahnke⁵⁸, S. Kermiche⁴⁵, A. Kiessling⁵⁴, M. Kilbinger⁵, B. Kubik³⁶, K. Kuijken¹, M. Kunz⁵⁹, H. Kurki-Suonio^{60,61}, A. M. C. Le Brun⁶², S. Ligori²⁸, P. B. Lilje⁵³, V. Lindholm^{60,61}, I. Lloro⁶³, G. Mainetti⁶⁴, O. Mansutti¹⁶, O. Marggraf⁶⁵, M. Martinelli^{7,8}, N. Martinet⁶⁶, F. Marulli^{67,20,21}, E. Medinaceli²⁰, M. Meneghetti^{20,21}, E. Merlin⁷, G. Meylan⁶⁸, A. Mora⁶⁹, M. Moresco^{67,20}, L. Moscardini^{67,20,21}, R. Nakajima⁶⁵, C. Neissner^{70,30}, S.-M. Niemi⁷¹, C. Padilla⁷⁰, S. Paltani⁴³, F. Pasian¹⁶, K. Pedersen⁷², W. J. Percival^{73,74,75}, V. Pettorino⁷¹, S. Pires⁵, G. Polenta⁷⁶, M. Poncet⁷⁷, L. A. Popa⁷⁸, F. Raison⁵⁰, A. Renzi^{79,80,20}, J. Rhodes⁵⁴, G. Riccio²⁵, E. Romelli¹⁶, M. Roncarelli²⁰, C. Rosset⁸¹, R. Saglia^{52,50}, Z. Sakr^{82,4,83}, A. G. Sánchez⁵⁰, D. Sapone⁸⁴, B. Sartoris^{52,16}, P. Schneider⁶⁵, T. Schrabback⁸⁵, A. Secroun⁴⁵, G. Seidel⁵⁸, E. Sihvola⁸⁶, P. Simon⁶⁵, C. Sirignano^{79,80}, G. Sirri²¹, A. Spurio Mancini⁸⁷, L. Stanco⁸⁰, P. Tallada-Crespi^{12,30}, I. Tereno^{41,88}, S. Toft^{89,90}, R. Toledo-Moreo⁹¹, F. Torradeflot^{30,12}, J. Valiviita^{60,61}, T. Vassallo^{16,49}, G. Verdoes Kleijn⁹², Y. Wang⁹³, J. Weller^{52,50}, F. M. Zerbi¹⁴, E. Zucca²⁰, M. Ballardini^{94,95,20}, M. Bolzonella²⁰, E. Bozzo⁴³, C. Burigana^{96,47}, R. Cabanac⁴, M. Calabrese^{97,29}, A. Cappi^{98,20}, T. Castro^{16,17,15,99}, J. A. Escartin Vigo⁵⁰, L. Gabarra¹⁰⁰, J. García-Bellido⁸², J. Macias-Perez¹⁰¹, R. Maoli^{102,7}, J. Martín-Fleitas¹⁰³, N. Mauri^{104,21}, R. B. Metcalf^{67,20}, P. Monaco^{105,16,17,15}, A. Pezzotta¹⁴, M. Pöntinen⁶⁰, I. Risso^{14,23}, V. Scottez^{106,107}, M. Sereno^{20,21}, M. Tenti²¹, M. Tucci⁴³, M. Viel^{15,16,18,17,99}, M. Wiesmann⁵³, Y. Akrami^{82,108}, I. T. Andika⁴⁹, G. Angora^{25,94}, S. Anselmi^{80,79,109}, M. Archidiacono^{110,111}, F. Atrio-Barandela¹¹², L. Bazzanini^{94,20}, J. Bel¹¹³, D. Bertacca^{79,51,80}, M. Bethermin¹¹⁴, F. Beutler¹⁰, A. Blanchard⁴, L. Blot^{115,62}, M. Bonici^{73,29}, M. L. Brown³⁴, S. Bruton¹¹⁶, B. Camacho Quevedo^{15,18,16}, F. Caro⁷, C. S. Carvalho⁸⁸, F. Cogato^{67,20}, S. Davini²³, F. De Paolis^{117,118,119}, G. Desprez⁹², A. Díaz-Sánchez¹²⁰, S. Di Domizio^{22,23}, J. M. Diego¹²¹, P. Dimauro^{122,7}, V. Duret⁴⁵, M. Y. Elkhashab^{105,16,17,15}, Y. Fang⁵², P. G. Ferreira¹⁰⁰, A. Finoguenov⁶⁰, A. Franco^{118,117,119}, K. Ganga⁸¹, T. Gasparetto⁷, E. Gaztanaga^{2,3,123}, F. Giacomini²¹, F. Gianotti²⁰, E. J. Gonzalez^{124,125}, G. Gozaliasl^{126,60}, A. Gruppuso^{20,21}, M. Guidi^{19,20}, C. M. Gutierrez^{33,127}, A. Hall¹⁰, C. Hernández-Monteagudo^{127,33}, H. Hildebrandt¹²⁸, J. Hjorth⁷², J. J. E. Kajava^{129,130,131}, Y. Kang⁴³, V. Kansal^{132,133}, D. Karagiannis^{94,134}, K. Kiiveri⁸⁶, J. Kim¹⁰⁰, C. C. Kirkpatrick⁸⁶, S. Kruk¹³, J. Le Graet⁴⁵, L. Legrand^{135,136}, M. Lembo¹³⁷, F. Lepori¹³⁸, G. Leroy^{139,140}, G. F. Lesci^{67,20}, J. Lesgourgues¹⁴¹, T. I. Liaudat¹⁴², M. Magliocchetti⁴⁶, F. Mannucci¹⁴³, C. J. A. P. Martins^{144,145}, L. Maurin⁴⁴, M. Miluzio^{13,146}, A. Montoro^{2,3}, C. Moretti^{16,15,17}, G. Morgante²⁰, S. Nadathur¹²³, K. Naidoo^{123,58}, A. Navarro-Alsina⁶⁵, S. Nesseris⁸², L. Pagano^{94,95}, D. Paoletti^{20,47}, F. Passalacqua^{79,80}, K. Paterson⁵⁸, L. Patrizii²¹, C. Pattison¹²³, A. Pisani⁴⁵, D. Potter¹⁴⁷, G. W. Pratt⁵, S. Quai^{67,20}, M. Radovich⁵¹, K. Rojas¹⁴⁸, W. Roster⁵⁰, S. Sacquegna¹⁴⁹, M. Sahlén¹⁵⁰, D. B. Sanders³², E. Sarpa^{18,99,16}, A. Schneider¹⁴⁷, E. Sellentin^{151,1}, L. C. Smith¹⁵², K. Tanidis¹⁵³, F. Tarsitano^{154,43}, R. Teyssier¹⁵⁵, A. Troja¹⁶, D. Vergani²⁰, F. Vernizzi¹⁵⁶, G. Verza^{157,158}, P. Vielzeuf⁴⁵, S. Vinciguerra⁶⁶, N. A. Walton¹⁵², A. H. Wright¹²⁸, and S.-S. Li^{159,160}

(Affiliations can be found after the references)

ABSTRACT

The *Euclid* galaxy survey will provide unprecedented constraints on cosmology, but achieving unbiased results will require an optimal characterisation and mitigation of systematic effects. Among these, the intrinsic alignments (IA) of galaxies are one of the dominant contaminants of the weak lensing (WL) and galaxy-galaxy lensing (GGL) probes. In this work, we assess IA modelling choices for *Euclid* DR1 3×2 pt analyses by comparing the performance of the two most commonly used IA models, nonlinear alignment (NLA) and tidal alignment tidal torquing (TATT), along with several variations. Our analyses combine three perspectives: i) the constraining power on the IA and cosmological parameters for each IA model, ii) the bias that results when the IA analysis model differs from the model used to generate the synthetic data vector, and iii) the degeneracies between IA and photometric redshift (photo- z) nuisance parameters. Among the IA models analysed, the redshift-dependent TATT model (z TATT) provides the most flexible description of IA, with a similar constraining power compared to simpler IA models, making it a well-motivated choice for *Euclid* DR1 3×2 pt analyses.

Key words. Cosmology: observations; Gravitational lensing: weak; large-scale structure of Universe; cosmological parameters

1. Introduction

Over the last decade, large galaxy surveys have provided us with vast amounts of data, allowing us to map the cosmic large-scale structure (LSS) with unprecedented precision. A key probe of this structure is weak lensing (WL; Kilbinger 2015; Mandelbaum 2018), which measures coherent distortions in the shapes of background galaxies caused by the intervening matter distribution. When combined with galaxy clustering (GC) and galaxy-galaxy lensing (GGL), these measurements form the so-called 3×2 pt analysis, which has been identified as one of the most powerful tools for constraining dark energy and testing cosmological models (Albrecht et al. 2006).

The first 3×2 pt cosmological analyses – performed by the Kilo-Degree Survey (KiDS; Kuijken et al. 2019), the Dark Energy Survey (DES; Dark Energy Survey Collaboration: Abbott et al. 2016), and the Hyper Suprime-Cam (HSC; Aihara et al. 2018) – provided state-of-the-art constraints on the Λ CDM and w_0w_a CDM cosmological models (Heymans et al. 2021; Abbott et al. 2022; More et al. 2023). Despite their impressive depth and area, these surveys remain largely statistically limited. This will no longer be the case for the new generation of galaxy surveys, such as *Euclid* (Euclid Collaboration: Mellier et al. 2025), the Vera C. Rubin Observatory Large Synoptic Survey Telescope (LSST; Ivezić et al. 2019), the Dark Energy Spectroscopic Instrument (DESI; DESI Collaboration: Abazajian et al. 2022) and the *Nancy Grace Roman* Space Telescope (Spergel et al. 2015), which will reach fainter magnitudes and cover even larger areas. For these surveys, statistical uncertainties will be subdominant, and cosmological inference will instead be limited by systematic effects if these are not accurately modelled.

Multiple systematic sources affect 3×2 pt analyses (Euclid Collaboration: Blot et al. 2025), including observational systematics, such as redshift uncertainties and shape estimation biases. While *Euclid* is designed to minimise these, the analyses can also be impacted by astrophysical systematics, such as magnification, baryonic effects, and the intrinsic alignments (IA) of galaxies. Here, we focus on IA (see Chisari 2025 for a review on the topic), one of the most challenging contaminants, arising from the intrinsic correlations in galaxy orientations that are caused by gravitational interactions with the surrounding LSS. These can mimic WL and GGL signals and thus bias cosmological constraints.

A variety of IA models aim to describe this effect. The most popular ones are the nonlinear alignment (NLA; Hirata et al. 2007; Bridle & King 2007) and the tidal alignment tidal torquing (TATT; Blazek et al. 2019) models, which are based on perturbative expansions of the gravitational tidal field, up to first and second order, respectively, and are extended into hybrid models

by evaluating them using nonlinear matter power spectra. Other more complex models attempt to describe IA by performing perturbation theory in Lagrangian (Chen & Kokron 2024; DeRose & Chen 2025), hybrid Lagrangian (Maion et al. 2024), or Eulerian (Vlah et al. 2020, 2021; Bakx et al. 2023) space. Extensions, such as the halo model (Schneider et al. 2010; Fortuna et al. 2021) can be used to describe IA at small scales. To date, the NLA and the TATT models have been the ones adopted in 3×2 pt analyses in previous surveys, given their ability to describe IA based on the uncertainties of these surveys. In particular, the TATT model was adopted by DES for their Y3 results (Abbott et al. 2022), while NLA (and variations of it) was adopted by KiDS (Hildebrandt et al. 2017; Asgari et al. 2021; Li et al. 2023; Wright et al. 2025b) and DES Y1 results (Abbott et al. 2018).

This is the third of a series of three papers aimed at studying IA in *Euclid*. The first paper (Euclid Collaboration: Hoffmann et al. 2026) describes the implementation of IA in the Flagship simulation (Euclid Collaboration: Castander et al. 2025). The second paper (Euclid Collaboration: Paviot et al. 2026, hereafter P26) demonstrates that IA models, particularly NLA and TATT, are able to fit the IA from Flagship, providing similar constraints as in observations, while also characterising the IA signal for different galaxy properties. Building on these results, the main objective of this third paper is to inform the best IA model choice for *Euclid*'s first data release (DR1) analysis.

We consider three different perspectives to accomplish this goal. First, we study the constraining power of NLA and TATT. As TATT is a more flexible model than NLA, it is expected to allow for a more accurate description of IA at small scales. However, if the small scales do not include significant additional information, the higher-order terms will not be constrained, reducing the constraining power, due to the larger number of parameters with respect to NLA. Here, we want to quantify if this loss of constraining power is significant. Even though our fiducial setup consists of 3×2 pt analyses, we also include WL-only and 2×2 pt (GC and GGL) constraining power analyses, as well as some variations in the assumed cosmological model, scale cuts and priors on the IA parameters. Secondly, we quantify the impact of IA mismodelling, which refers to the scenario where a data vector follows a certain IA model, but is modelled with a different one. Since we do not know the true model that best describes IA in the Universe, it is necessary to quantify the potential biases that mismodelling IA can induce, not only in the IA parameters, but also in the cosmological ones (Campos et al. 2023; Samuroff et al. 2024; Paopiamsap et al. 2024). Finally, we evaluate the degeneracies between IA and photometric redshift (photo- z) estimates, since these degeneracies can mask or undermine the effect that IA have on cosmological analyses (Li et al. 2021; Fischbacher et al. 2023; Leonard et al. 2024; Mill

* e-mail: navarrogirones@strw.leidenuniv.nl

et al. 2025) and provide some recommendations on how to avoid them.

The paper is structured as follows. In Sect. 2, we present the modelling description used to describe the angular power spectra and the IA of galaxies. In Sect. 3, we introduce the forecasting pipeline, describing the likelihood, the sampled parameters and their priors, the employed covariance matrix, and the scale cuts. In Sect. 4, we describe the measurement of the values of the IA parameters from the Flagship simulation and how the synthetic data vectors are generated. The main results showing the constraining power, the IA mismodelling effect, and the degeneracies of IA with photo-zs are presented in Sect. 5. We finish with the conclusions in Sect. 6.

2. Modelling

Here, we describe the theoretical setup for modelling a 3×2 pt analysis in harmonic space by defining the harmonic angular power spectra (Sect. 2.1). We also pay particular attention to different approaches to model IA (Sect. 2.2).

2.1. Angular power spectra

We model the cross-correlation of different observables that are split in redshift bins. In the Limber approximation (Limber 1953), and assuming a flat universe, this can be accomplished by writing the angular power spectra in harmonic space as

$$C_{ij}^{AB}(\ell) = \int_0^{\chi_{\text{hor}}} d\chi \frac{W_i^A(\chi) W_j^B(\chi)}{\chi^2} P_{AB} \left(k = \frac{\ell + 1/2}{\chi}, z(\chi) \right), \quad (1)$$

where A and B indicate the tracers that are correlated, and P_{AB} their corresponding power spectra, as summarised in Table 1. Here, $P_{\delta\delta}$ corresponds to the matter power spectrum, while P_{ol} and P_{II} are the IA power spectra described in Sect. 2.2. The conversions for $P_{g\delta}$, P_{gl} , and P_{gg} in Table 1 assume a linear galaxy bias modelling approach (Kaiser 1984), with b_1 the linear galaxy bias term¹, which relates the mean overdensities of galaxies and mass. χ_{hor} corresponds to the comoving distance χ at the horizon. The kernels $W_i^A(\chi)$ and $W_j^B(\chi)$ depend on the observables of interest, and the subscripts i and j to the redshift bins of the tracers.

The angular power spectrum in harmonic space for the observed cosmic shear (LL) consists of a purely WL contribution ($\gamma\gamma$), a contribution from IA (II) and a combination of both (Iy and γI). These contributions can be written as

$$C_{ij}^{\text{LL}}(\ell) = C_{ij}^{\gamma\gamma}(\ell) + C_{ij}^{\gamma\text{I}}(\ell) + C_{ij}^{\text{Iy}}(\ell) + C_{ij}^{\text{II}}(\ell), \quad (2)$$

where the subscripts i, j correspond to the source tomographic redshift bins. In the case of $A = \gamma$, $W_i^\gamma(\chi)$ corresponds to the WL weighting function

$$W_i^\gamma(\chi) = \frac{3H_0^2\Omega_m}{2c^2} \frac{\chi}{a(\chi)} \int_z^{z_{\text{max}}} d\chi' n_i^S(z(\chi')) \frac{dz'}{d\chi'} \frac{\chi' - \chi}{\chi'}, \quad (3)$$

with H_0 the Hubble constant, c the speed of light, a the scale factor, z_{max} the maximum redshift of the survey, and n_i^S the source redshift distribution. In the case of $A = \text{I}$, the kernel becomes

$$W_i^{\text{I}}(\chi) = n_i^S(z) \frac{dz}{d\chi}. \quad (4)$$

¹ As justified in Sect. 3.2, we leave more complex galaxy bias relations for future work.

Table 1. Power spectra cases depending on the AB combination in Eq. (1). The indexes δ , γ , μ , I and g refer to the density, shear, magnification, intrinsic shape and galaxy components, respectively.

AB	P_{AB}
$\gamma\gamma, \mu\gamma, \mu\mu$	$P_{\delta\delta}$
$\gamma\text{I}, \text{Iy}, \text{I}\mu$	$P_{\delta\text{I}}$
II	P_{II}
$\gamma\gamma, \text{g}\mu, \mu\text{g}$	$P_{\text{g}\delta} = b_1 P_{\delta\delta}$
gI	$P_{\text{gI}} = b_1 P_{\delta\text{I}}$
gg	$P_{\text{gg}} = b_1^2 P_{\delta\delta}$

The observed GGL angular power spectrum (GL) arises from contributions from the distortions of WL by foreground galaxies ($\gamma\gamma$), together with smaller contributions from IA (originated from source galaxies located nearby lens galaxies, denoted as gI) and magnification bias, which correlates with both WL ($\mu\gamma$) and IA (μI). The total observed GGL signal can be described as

$$C_{ij}^{\text{GL}} = C_{ij}^{\text{g}\gamma}(\ell) + C_{ij}^{\text{gI}}(\ell) + C_{ij}^{\mu\gamma}(\ell) + C_{ij}^{\mu\text{I}}(\ell), \quad (5)$$

where the subscripts i, j correspond to the tomographic redshift bins from sources and lenses, respectively. Now, for $A = \text{g}$ the kernel becomes

$$W_i^{\text{g}}(\chi) = n_i^{\text{L}}(z) \frac{dz}{d\chi}, \quad (6)$$

with $n_i^{\text{L}}(z)$ the lens redshift distribution. In the case of $A = \mu$, the kernel for magnification is

$$W_i^\mu(\chi) = 2(\alpha_i - 1)W_i^\gamma(\chi), \quad (7)$$

where $\alpha_i = 5s_i/2$, with s_i the logarithmic slope of the magnitude distribution of the lenses.

Finally, the observed GC angular power spectrum (GG) originates from purely galaxy-galaxy (gg) and magnification-magnification ($\mu\mu$) contributions, together with a combination from both (g μ and μg):

$$C_{ij}^{\text{GG}} = C_{ij}^{\text{gg}}(\ell) + C_{ij}^{\text{g}\mu}(\ell) + C_{ij}^{\mu\text{g}}(\ell) + C_{ij}^{\mu\mu}(\ell), \quad (8)$$

where now the subscripts i, j correspond to the lens redshift bins. In our study, we only consider the GG auto-correlations of lens redshift bins, since the contribution from cross-correlations is expected to be subdominant, their inclusion might introduce additional systematics (Porredon et al. 2021), and the computation time is decreased by ignoring them.

We note that we have made some assumptions in Eqs. (2), (5), and (8) to simplify our analyses. In particular, we have neglected the contribution of magnification to the WL C_ℓ (Deshpande et al. 2020) and we have not considered redshift-space distortions (RSD; Kaiser 1987). Although all these effects are important for precision cosmology (Euclid Collaboration: Tassis et al. 2024; Euclid Collaboration: Mathewson et al. 2025), they are subdominant contributions, which we chose to neglect to focus on the effect of IA.

2.2. Models for intrinsic alignment of galaxies

In this section, we present the NLA and TATT models, and variations of them. We do not explore more complex models given that DR1, while expecting a significant improvement over previous surveys, will still deliver only a fraction of the final mission's constraining power.

2.2.1. NLA

The simplest model describing the IA of galaxies involves a relation between the shape of the galaxies and the tidal field of their surrounding LSS. This leads to a linear response to the tidal field, as first proposed in the Linear Alignment (LA) model (Catelan et al. 2001; Hirata & Seljak 2004). In this scenario, the intrinsic shear of a galaxy is described by

$$\gamma^I = -\frac{\bar{C}_1}{4\pi G_N} (\Delta_x^2 - \Delta_y^2, 2\Delta_x\Delta_y) S[\psi_P], \quad (9)$$

where $\bar{C}_1 = 5 \times 10^{-14} M_\odot^{-1} h^{-2} \text{Mpc}^3$ is a normalisation factor calibrated by Brown et al. (2002) using low-redshift observations from the SuperCOSMOS survey (Hambly et al. 2001), G_N is the Newtonian gravitational constant, x and y are the Cartesian coordinates in the plane of the sky, S is a smoothing function applied to the Newtonian potential ψ_P at the epoch of galaxy formation, and Δ corresponds to the comoving spatial derivative.

From Eq. (9), the intrinsic-intrinsic (P_{II}) and matter-intrinsic ($P_{\delta I}$) power spectra can be defined, respectively, as

$$\begin{aligned} P_{II}(z, k) &= C_1^2(z) P_{\delta\delta}(z, k), \\ P_{\delta I}(z, k) &= C_1(z) P_{\delta\delta}(z, k), \end{aligned} \quad (10)$$

where, assuming a power-law dependence with redshift, $C_1(z)$ can be written as

$$C_1(z) = -A_1 \bar{C}_1 \frac{\Omega_m \rho_{\text{crit}}}{D(z)} \left(\frac{1+z}{1+z_0} \right)^{\eta_1}, \quad (11)$$

with ρ_{crit} the critical density today, $D(z)$ the growth factor, and z_0 the pivoting redshift. The free parameters A_1 and η_1 indicate the overall amplitude and the redshift dependence, respectively. In the LA model, $P_{\delta\delta}$ in Eq. (10) corresponds to the linear matter power spectrum. However, the NLA model (Hirata et al. 2007; Bridle & King 2007) proposes the substitution of the linear by the nonlinear matter power spectrum, which allows for a better description of the observed IA signal. Although this is not a theoretically motivated approach, NLA constitutes one of the most frequently used IA models. As such, we adopt it as one of the IA models used in this work. In particular, we consider two scenarios within this model, the minimal NLA (which we will simply refer to as NLA, if not specified otherwise) and the z NLA models, satisfying $\eta_1 = 0$ and $\eta_1 \neq 0$, respectively.

2.2.2. TATT

A more complex IA model can be derived by performing perturbative expansions of the intrinsic shear field, γ_{ij}^I , in terms of the matter density field, δ_m , and the tidal field tensor, s_{ij} . By expanding up to second order, we obtain the intrinsic shear field as described by the TATT model (Blazek et al. 2019)

$$\gamma_{ij}^I = C_1 s_{ij} + C_{1\delta} \delta_m s_{ij} + C_2 \left(\sum_k s_{ik} s_{kj} - \frac{1}{3} \delta_{ij} s^2 \right) + \dots, \quad (12)$$

where the first term reduces to the general NLA model, the second term can be related to the fact that we only observe IA at the positions of the galaxies, and the third term describes the tidal torquing effect, which is thought to explain the angular momentum-driven IA of spiral galaxies. The term $s^2 \equiv s^{ij} s_{ij}$, where we have assumed Einstein notation.

Within the TATT model, the intrinsic shear field naturally decomposes into E - and B -mode contributions. The linear tidal-alignment term generates only E -modes, as in the NLA model,

Table 2. IA models considered in this work.

IA model	Free parameters
NLA	A_1
z NLA	A_1, η_1
k NLA	$A_1, \eta_1, A_{1\delta}$
TATT	$A_1, A_2, A_{1\delta}$
z TATT- b_1	A_1, A_2, η_1, η_2
z TATT	$A_1, A_2, A_{1\delta}, \eta_1, \eta_2$

while the density-weighted and quadratic tidal-torquing terms introduce additional E -mode power and also generate B -modes. Evaluated at one-loop order, the expressions of the E - and B -mode intrinsic-intrinsic power spectra, are given, respectively, by

$$\begin{aligned} P_{II}^{EE}(z, k) &= C_1^2(z) P_{\delta\delta}(z, k) \\ &+ 2C_1(z) C_{1\delta}(z) D^4(z) [A_{0|0E}(k) + C_{0|0E}(k)] \\ &+ C_{1\delta}^2(z) D^4(z) A_{0E|0E}(k) + C_2^2(z) D^4(z) A_{E2|E2}(k) \\ &+ 2C_1(z) C_2(z) D^4(z) [A_{0|E2}(k) + B_{0|E2}(k)] \\ &+ 2C_{1\delta}(z) C_2(z) D^4(z) D_{0E|E2}(k), \end{aligned} \quad (13)$$

$$\begin{aligned} P_{II}^{BB}(z, k) &= C_{1\delta}^2(z) A_{0B|0B}(k) \\ &+ C_2^2(z) A_{B2|B2}(k) + 2C_{1\delta}(z) A_2(z) D_{0B|B2}(k), \end{aligned} \quad (14)$$

while the matter-intrinsic power spectrum is

$$\begin{aligned} P_{\delta I}(z, k) &= C_1(z) P_{\delta\delta}(z, k) + C_{1\delta}(z) D^4(z) [A_{0|0E}(k) + C_{0|0E}(k)] \\ &+ C_2(z) D^4(z) [A_{0|E2}(k) + B_{0|E2}(k)], \end{aligned} \quad (15)$$

where $C_1(z)$ corresponds to the one introduced in Eq. (11) and

$$C_2(z) = 5A_2 \bar{C}_1 \frac{\Omega_m \rho_{\text{crit}}}{D^2(z)} \left(\frac{1+z}{1+z_0} \right)^{\eta_2}, \quad (16)$$

$$C_{1\delta}(z) = A_{1\delta} C_1(z),$$

with $A_1, A_2, A_{1\delta}, \eta_1$, and η_2 being the free TATT parameters. The one-loop order terms in Eqs. (13–15) are defined in Blazek et al. (2019).

Note that the A_1 and η_1 parameters are shared with the z NLA model, which is recovered in the case where $A_2 = \eta_2 = A_{1\delta} = 0$. We consider four cases for the TATT model in this work: the minimal TATT model (which we will simply refer to as TATT, if not specified otherwise), with $\eta_1 = \eta_2 = 0$; the z TATT model, with $\eta_1 \neq 0$ and $\eta_2 \neq 0$; the z TATT- b_1 model, with $\eta_1 \neq 0$, $\eta_2 \neq 0$, and $A_{1\delta} = b_1 = 1$, where b_1 is the linear galaxy bias of source galaxies, assumed to be one (Troxel et al. 2018; Samuroff et al. 2019); and the k NLA model (Wright et al. 2025b), with $A_2 = \eta_2 = 0$, which can also be thought of as an extension of the z NLA model. Table 2 summarises the different IA models employed in this work, specifying their free parameters.

3. Forecast pipeline

In this section, we present the pipeline used to forecast the impact of IA on the baseline 3×2 pt *Euclid* analyses. We first describe how we build and sample the likelihood. Next, we introduce the set of parameters sampled in the analysis, justifying

their fiducial values and priors. We later describe how the covariance matrix is built and, finally, we present the scale-cut choices that we employ.

The analysis is performed with the *CosmoSIS*² code (Zuntz et al. 2015), which allows us to compute the theoretical predictions introduced in Sect. 2 in a module-like setup, where users can specify their modelling choices. *CosmoSIS* connects the theoretical predictions with samplers, that allow us to explore the parameter space, given a specific data vector (DV), covariance matrix, and scale cuts. The linear matter power spectrum and other underlying background quantities are computed using the *CAMB* Boltzmann solver code (Lewis et al. 2000; Howlett et al. 2012). We employ two different recipes for the computation of the nonlinear matter power spectrum. For the generation of synthetic DVs in Sect. 4.4, with which we perform the core of the analysis, we use the *HMCode-2020* implementation with baryonic feedback (Mead et al. 2021), which allows for complete coverage of the range in cosmological parameters. For the determination of the IA parameters in the Flagship simulation (see Sect. 4.3) we use the *EuclidEmulator2*³ (Euclid Collaboration: Knabenhans et al. 2021), since it more accurately describes the signal measured in Flagship. The one-loop terms in Eqs. (13–15) are computed using the *FAST-PT* code (McEwen et al. 2016; Fang et al. 2017), which uses an integration based on Fast Fourier Transform (FFT) methods to accelerate the computation.

While in this work we use *CosmoSIS*, we note that the Euclid Consortium is developing its own inference pipeline (*cloelib* and *cloelike*), that will be publicly hosted prior to the first *Euclid* cosmology analysis at the GitHub organisation *cloe-org*⁴ (Cañas-Herrera et al. 2025). This pipeline builds upon previous work published in Euclid Collaboration: Cardone et al. (2025), Euclid Collaboration: Joudaki et al. (in preparation), Euclid Collaboration: Cañas-Herrera et al. (2025), Euclid Collaboration: Martinelli et al. (2025), Euclid Collaboration: Goh et al. (2025), Euclid Collaboration: Blot et al. (2025).

3.1. Likelihood

Given a DV, \mathbf{D} , and a theoretical vector given by a model M , \mathbf{T}_M , we perform a likelihood analysis to constrain a set of parameters of interest, \mathbf{p} . We define a Gaussian likelihood L , such that

$$\ln L(\mathbf{D}|\mathbf{p}, M) = -\frac{1}{2} \left[(\mathbf{D} - \mathbf{T}_M)^T \mathbf{C}^{-1} (\mathbf{D} - \mathbf{T}_M) \right] + C, \quad (17)$$

where \mathbf{C} corresponds to the covariance matrix of the data, presented in Sect. 3.3, and C is a normalisation constant. The DV in our analysis is given by

$$\mathbf{D} = \left\{ C_{ij}^{\text{LL}}(\ell), C_{ij}^{\text{GL}}(\ell), C_{ij}^{\text{GG}}(\ell) \right\}, \quad (18)$$

which represents the concatenation of the theoretical quantities defined in Eqs. (2–8) evaluated at the fiducial values in the parameter space \mathbf{p} , and is presented in Sect. 4. Given that \mathbf{D} is a synthetic DV, the theoretical vector \mathbf{T}_M has a similar definition as in Eq. (18), with the difference that it is not necessarily evaluated at the fiducial values of \mathbf{p} , but on any value in the parameter space

$$\mathbf{T}_M = \left\{ C_{ij}^{\text{LL}}(\ell|\mathbf{p}), C_{ij}^{\text{GL}}(\ell|\mathbf{p}), C_{ij}^{\text{GG}}(\ell|\mathbf{p}) \right\}. \quad (19)$$

² <https://github.com/joezuntz/cosmosis>

³ <https://github.com/miknab/EuclidEmulator2>

⁴ <https://github.com/cloe-org>

The posterior probability distribution of the set of parameters \mathbf{p} , which indicates how likely different values of the parameters are, given a DV and an assumed model, is provided by Bayes' theorem as

$$P(\mathbf{p}|\mathbf{D}, M) = \frac{L(\mathbf{D}|\mathbf{p}, M)P(\mathbf{p}|M)}{P(\mathbf{D}|M)}, \quad (20)$$

where $P(\mathbf{p}|M)$ is the prior probability distribution and $P(\mathbf{D}|M)$ is the Bayesian evidence.

To sample the posterior distribution, we employ the *NAUTILUS* sampler (Lange 2023), which is implemented in *CosmoSIS*. *NAUTILUS* employs importance nested sampling techniques (Feroz et al. 2019), an extension of traditional nested sampling methods (Skilling 2004). The latter technique allows us to compute the Bayesian evidence and it samples the posterior distribution as a by-product, while the former improves the process by keeping all likelihood evaluations and, in the case of *NAUTILUS*, efficiently sampling the posterior distribution using neural networks. The *NAUTILUS* configuration we use discards the points drawn in the exploration phase. We rely on 6000 live points and require a minimum effective sample size of $N_{\text{eff}} = 15\,000$, with 1200 likelihood evaluations at each step. We use 16 neural networks in each network ensemble.

3.2. Parameters and priors

We constrain the posterior probability distributions of the parameters of interest for two cosmological models: flat Λ CDM and w_0w_a CDM. The latter is characterised by a redshift-dependent dark energy equation-of-state parameter $w(z) = w_0 + w_a(1 - a)$ (Chevallier & Polarski 2001; Linder 2003), where w_0 is the equation of state today, and w_a quantifies the dependence with redshift. The Λ CDM model corresponds to the special case where $w_0 = -1$ and $w_a = 0$. We vary three cosmological parameters for the flat Λ CDM case: the total matter density in units of physical density, $\Omega_m h^2$, the Hubble parameter, h , and the amplitude of the primordial scalar density perturbations, A_s . In the case of w_0w_a CDM, in addition to these three cosmological parameters, we also vary w_0 and w_a . We fix the values of the other cosmological parameters to reduce computation time, since these are not that well constrained by 3×2 pt analyses. However, we note that in real data analysis, these parameters are usually sampled. We fix both the baryonic and the curvature density in physical units, $\Omega_b h^2$ and $\Omega_k h^2$, the spectral index of the primordial power spectrum, n_s , and the optical depth of reionisation, τ . We set the number of massive neutrinos to one, with $N_{\text{eff}} = 3.046$ and $\Sigma m_\nu = 0.06 \text{ eV}/c^2$, where this minimum mass arises from that allowed by oscillation experiments (Patrignani et al. 2016). *CosmoSIS* also allows deriving some extra cosmological parameters, such as σ_8 and $S_8 \equiv \sigma_8 \sqrt{\Omega_m/0.3}$, where the former quantifies the amplitude of matter perturbations and the latter captures the $\Omega_m - \sigma_8$ degeneracy that WL measurements are most sensitive to.

In addition to the cosmological parameters, we also consider other systematic and astrophysical parameters. The number of parameters sampled to capture IA will depend on the IA model we consider, as shown in Table 2. We set the pivoting redshift to $z_0 = 0.62$, in accordance with P26. Baryon feedback is included based on the active galactic nuclei (AGN) feedback strength, modelled via the sub-grid heating parameter, T_{AGN} . We assume a linear galaxy bias approach, with b_i the linear galaxy bias per lens bin i . This way, we focus on the effect of IA and avoid opening up the parameter space with more complex galaxy bias relations, such as a nonlinear galaxy bias approach (Desjacques

et al. 2018), which is left for future work. To take into account the uncertainty in the shear calibration procedure, we use a multiplicative shear bias factor per source tomographic redshift bin, m_i , relating the observed and the true shear, such that

$$\gamma_i^{\text{obs}} = (1 + m_i) \gamma_i^{\text{true}}, \quad (21)$$

which will, in turn, modify the angular power spectra (Kitching et al. 2019) described in Eqs. (2) and (5) by

$$C_{ij}^{\text{LL}}(\ell) \rightarrow (1 + m_i)(1 + m_j)C_{ij}^{\text{LL}}(\ell), \quad (22)$$

$$C_{ij}^{\text{GL}}(\ell) \rightarrow (1 + m_i)C_{ij}^{\text{GL}}(\ell). \quad (23)$$

We do not consider an additive bias term, since this can be estimated and subtracted from the data (Kitching et al. 2019; Hoekstra 2021).

Any photo- z biases are parametrised by considering a shift (Δz) in the mean of the $n(z)$ redshift distribution of both sources and lenses, such that

$$n_i(z) \rightarrow n_i(z - \Delta z_i), \quad (24)$$

where Δz_i is set for each redshift bin. Finally, we also sample the magnification bias parameter, α_i , introduced in Eq. (7). Considering that our DR1 setup comprises 6 lens and 6 source tomographic redshift bins (see Sect. 4.2), this analysis leads to 34 sampled parameters (without considering w_0 and w_a) which, in combination with the IA ones, amount to 35–39 in the case of ΛCDM and 37–41 in the case of $w_0w_a\text{CDM}$, depending on the assumed IA model.

Table 3 shows the fiducial values and priors for all parameters considered in this analysis. In the case of the cosmological parameters, we follow the fiducial values from the Flagship simulation (Euclid Collaboration: Castander et al. 2025) and the priors derived in the DES Y3 3×2 pt analysis (Abbott et al. 2022). The values of the IA parameters are also derived from the Flagship simulation and further justified in Sect. 4.3. The IA priors are assumed to be broad, although in Sect. 5.1.4 we show the negligible effect of narrowing the IA priors in our analyses. For the halo model parameter, we assume the prior range of the combined BAHAMAS (McCarthy et al. 2017) and COSMO-OWLS (Le Brun et al. 2014) case, extracted from the halo model HMCODE-2020 (Mead et al. 2021), while we choose a fiducial value widely used in Mead et al. (2021). We derive the galaxy bias parameters by fitting the angular correlation function, $w(\theta)$, to the sample used in this analysis (Sect. 4.2), and set broad priors to recover the fiducial. The priors of the remaining parameters are defined as Gaussian, $\mathcal{N}(\mu, \sigma)$, with μ representing the mean and σ the standard deviation. The priors of the multiplicative shear bias are based on the expected uncertainties for *Euclid* DR1. A similar scenario occurs for the priors on the source and lens photo- z errors, which are defined as $\Delta z_s^i = 0.01(1 + z_s)$, so that they are of the same order as the final stage-III photo- z priors (e.g., Wright et al. 2025a), and which are also expected to be similar to those of *Euclid* DR1. Finally, in the case of the magnification bias, the fiducial values are computed from the slope of the cumulative number counts at the magnitude cut of the lenses defined in Sect. 4.2, while the priors are defined as broad to recover the fiducial.

3.3. Covariance matrix

We compute the covariance matrix using the Spaceborne code⁵ (Euclid Collaboration: Sciotti et al., in preparation), which has

Table 3. Model parameters, fiducial values and priors used for the ΛCDM and $w_0w_a\text{CDM}$ analyses. Priors between brackets correspond to flat priors, while priors indicated with $\mathcal{N}(\mu, \sigma)$ are Gaussian priors, with mean μ and standard deviation σ .

Parameter	Fiducial	Prior
Cosmology		
$\Omega_m h^2$	0.143	[0.045, 0.404]
h	0.67	[0.55, 0.91]
$A_s \times 10^9$	2.1	[0.5, 5.0]
$\Omega_b h^2$	0.022	Fixed
$\Omega_k h^2$	0.0	Fixed
n_s	0.96	Fixed
w_0	-1.0	Fixed or [-2.0, -0.333]
w_a	0.0	Fixed or [-3.0, 3.0]
τ	0.0697186	Fixed
Intrinsic alignments		
A_1	0.92	[0.0, 3.0]
A_2	0.40	[-2.0, 2.0]
η_1	2.26	[0.0, 4.0]
η_2	2.69	[-6.0, 6.0]
A_{16}	-0.83	[-5.0, 3.0]
z_0	0.62	Fixed
Halo model parameters		
$\log_{10}(T_{\text{AGN}}/\text{K})$	7.8	[7.6, 8.3]
Galaxy bias		
b_i	1.14, 1.20, 1.32, 1.42, 1.52, 1.94	[0.8, 3.5]
Multiplicative shear bias		
m_i	0.0	$\mathcal{N}(0.0, 0.01)$
Source photo-z errors		
Δz_s^1	0.0	$\mathcal{N}(0.0, 0.014)$
Δz_s^2	0.0	$\mathcal{N}(0.0, 0.016)$
Δz_s^3	0.0	$\mathcal{N}(0.0, 0.018)$
Δz_s^4	0.0	$\mathcal{N}(0.0, 0.020)$
Δz_s^5	0.0	$\mathcal{N}(0.0, 0.023)$
Δz_s^6	0.0	$\mathcal{N}(0.0, 0.028)$
Lens photo-z errors		
Δz_l^1	0.0	$\mathcal{N}(0.0, 0.013)$
Δz_l^2	0.0	$\mathcal{N}(0.0, 0.014)$
Δz_l^3	0.0	$\mathcal{N}(0.0, 0.016)$
Δz_l^4	0.0	$\mathcal{N}(0.0, 0.017)$
Δz_l^5	0.0	$\mathcal{N}(0.0, 0.019)$
Δz_l^6	0.0	$\mathcal{N}(0.0, 0.023)$
Magnification bias		
α_1	0.516	[0.1, 1.0]
α_2	0.682	[0.1, 1.5]
α_3	0.652	[0.1, 1.5]
α_4	0.804	[0.1, 2.0]
α_5	1.178	[0.1, 2.5]
α_6	1.972	[0.1, 4.0]

been specifically designed to produce covariance matrices for the *Euclid* mission. Three terms contribute to the total covariance matrix of this work: Gaussian covariance, super-sample covariance, and connected non-Gaussian covariance. The Gaussian covariance accounts for the case where the fields under study are Gaussian distributed, which is a good approximation for large angular scales. This is proportional to the squared amplitude of the observables. The super-sample covariance allows for the inclusion of super-survey modes, which couple with the in-survey modes observed by *Euclid*. In particular, the super-sample covariance implemented in Spaceborne is computed taking into account the cross-covariance of the super-survey modes at different redshifts. Finally, the connected non-Gaussian covariance accounts for the coupling of in-survey modes. This term is most relevant at small scales, where the assumption of Gaussianity of the power spectra is not satisfied, due to nonlinear gravitational interactions. The relevant equations employed for the covariance computation can be found in Euclid Collaboration: Sciotti et al. (in preparation). The shape noise, sky fraction, and number den-

⁵ <https://github.com/davidesciotti/Spaceborne>

sities of sources and lenses – necessary for the computation of the covariance matrix – are specified in Sect. 4.2.

3.4. Scale cuts

Since current theories become unreliable on small, highly non-linear scales, we impose scale cuts to ensure we only use scales where predictions are robust. We set scale cuts based on Doux et al. (2021, 2022), who define a small-scale physical mode, k_{\max} , that is converted to a multipole ℓ_{\max} using the relation $k = (\ell + 1/2)/\chi(z)$. The idea behind this technique is that the matter power spectra that enter Eq. (1) are valid for $k < k_{\max}$, so that we effectively remove multipoles ℓ receiving information from smaller scales. This is done by integrating the C_{ℓ} up to a given k_{\max} , such that the fraction over the total C_{ℓ} is $\alpha < 1$:

$$\int_{-\infty}^{\ln k_{\max}} d \ln k \frac{dC_{\ell}}{d \ln k} = \alpha C_{\ell}. \quad (25)$$

We set $\alpha = 0.95$, so that the wavenumbers $k > k_{\max}$ only contribute 5% to the total C_{ℓ} . We consider different k_{\max} based on the cosmological probe we analyse. We set $k_{\max} = 0.3 h \text{ Mpc}^{-1}$ for GGL and GC, since we want to stay in a regime where linear galaxy bias is valid.⁶ For WL, we define two scale cuts, $k_{\max} = 1 h \text{ Mpc}^{-1}$ and $k_{\max} = 3 h \text{ Mpc}^{-1}$, to test how the constraining power varies when including smaller scales. In this way, we capture the regime where systematic uncertainties are subdominant with respect to statical ones (Takahashi et al. 2012; Doux et al. 2021, 2022; Schaye et al. 2023; Euclid Collaboration: Knabenhans et al. 2021).

The scale cuts are derived from Eqs. (2–8), which describe the WL, GGL, and GC observables. We consider two scenarios: i) scale cuts for the determination of the IA values from the Flagship simulation (Sect. 4.3) and ii) scale cuts for the main analysis of this work. In the first case, since the Flagship simulation allows us to obtain positions without the effect of magnification, Eqs. (5–8) do not include the magnification contributions. In the second case, all the terms in Eqs. (2–8) are included. We note that the scale cuts will depend on the assumed IA model, so we compute different sets of scale cuts based on the model considered. However, we also note that the differences of scale cuts between IA models are not very significant.

Figure 1 shows the scale cuts in terms of ℓ_{\max} as a function of redshift for the WL case with $k_{\max} = 1 h \text{ Mpc}^{-1}$ and $k_{\max} = 3 h \text{ Mpc}^{-1}$, and for GGL and GC at $k_{\max} = 0.3 h \text{ Mpc}^{-1}$. For simplicity, we only show the scale cuts for the auto-correlation of tomographic redshift bins. In this case, we adopt the z NLA model and consider the effect of magnification. Note how the derived ℓ_{\max} for the WL probe increases when increasing the k_{\max} . We find that the ℓ_{\max} values derived for $k_{\max} = 1 h \text{ Mpc}^{-1}$ and $k_{\max} = 3 h \text{ Mpc}^{-1}$ are consistent with those reported in Doux et al. (2021, 2022), although they are more conservative than those in other *Euclid* forecasts (Euclid Collaboration: Blanchard et al. 2020; Taylor et al. 2021; Euclid Collaboration: Blot et al.

⁶ Euclid Collaboration: Gouyou Beauchamps et al. (in preparation) analyse the validity of the linear galaxy bias prescription in angular statistics for a *Euclid* sample defined in Flagship. The authors recommend defining a maximum $k_{\max} = 0.2 h \text{ Mpc}^{-1}$ to avoid significant deviations from the linear galaxy bias regime. However, given that this recommendation is made for the Flagship simulation, and the main analyses of this work are performed with synthetic DVs, the slightly more optimistic scale cut of $k_{\max} = 0.3 h \text{ Mpc}^{-1}$ that we employ will not yield any bias in our constraints, just a small increase in the constraining power for GGL and GC.

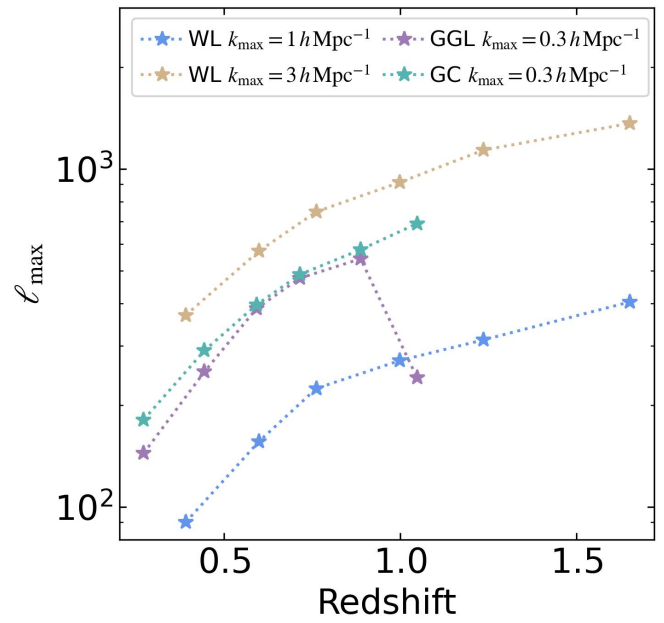


Fig. 1. Scale cuts for WL, GGL, and GC as a function of redshift for different k_{\max} . The assumed IA model is z NLA and magnification contributions are included.

2025). The drop in ℓ_{\max} in the last redshift bin for the GGL case is due to a large contribution to the C_{ℓ} from the magnification term. We tested determining the scale cuts when removing the magnification contributions (gI and μI) from Eq. (5) and the drop in ℓ_{\max} at high redshift did not appear.

4. Synthetic data vectors

Since the observed differences between the z NLA and z TATT models are highly dependent on the assumed values on the IA parameters, we first constrain these values from the Flagship simulation (Euclid Collaboration: Castander et al. 2025). This is a galaxy mock catalogue based on an N -body simulation, developed to reproduce the expected galaxy samples that *Euclid* will observe to help prepare its scientific analyses. Importantly for IA, Flagship was calibrated to match the observed correlation functions of IA (Euclid Collaboration: Hoffmann et al. 2026) from previous surveys. After measuring the IA values from Flagship, we generate synthetic data vectors assuming a *Euclid* DR1 setup.

4.1. Flagship simulation

The Flagship simulation⁷ is based on a state-of-the-art N -body simulation that evolved four trillion dark matter particles, generating a lightcone on-the-fly that covers one octant of the sky up to redshift $z = 3$ (Euclid Collaboration: Castander et al. 2025). From these dark matter particles, 16 billion dark matter haloes were identified with the ROCKSTAR halo finder (Behroozi et al. 2013). These haloes were populated with mock galaxies using halo occupation distribution (HOD) and abundance matching (AM) techniques. The parameters of the galaxy mock were calibrated to reproduce observed galaxy correlations and basic galaxy properties. Photo- z estimates were computed from the

⁷ accessible via <https://cosmohub.pic.es> (Carretero et al. 2017; Tallada et al. 2020).

expected observed fluxes and errors using the official *Euclid* pipeline, the Nearest Neighbours Photometric Redshifts (NNPZ; *Euclid* Collaboration: Tucci et al. 2025). As a result, the Flagship simulation provides a complete magnitude-limited sample down to $H_E < 26$, with 3.4 billion galaxies including several galaxy properties. The simulation assumes a Λ CDM cosmology with $\Omega_m = 0.319$, $\Omega_b = 0.049$, $h = 0.67$, $n_s = 0.96$, and $A_s = 2.1 \times 10^{-9}$.

The IA are implemented in the Flagship simulation following *Euclid* Collaboration: Hoffmann et al. (2026). This implementation takes place in two steps: modelling galaxy shapes and modelling galaxy orientations. First, each galaxy is approximated as a 3D ellipsoid and its axis ratios are assigned based on the galaxy redshift, colour, and magnitude. Then, these 3D ellipsoids are projected along the observer's line of sight (LOS) to obtain 2D galaxy shapes, and are calibrated to follow the galaxy shape distribution from the COSMOS survey (Laigle et al. 2016; Griffith et al. 2012). Second, the galaxy orientations are assigned separately for central and satellite galaxies, where the former have their principal axes aligned with those from the dark matter haloes in which they reside, while the latter have their major axes aligned towards the centre of their haloes. Furthermore, to accurately match the IA statistics in observations and simulations, one has to introduce a misalignment angle that reduces the alignment between the axes of galaxies and haloes. This misalignment angle depends on the galaxy type (central or satellite), colour, redshift, and magnitude.

4.2. Sample definition

To match the approximate upper-limit area expected for DR1, we define a 30-degree cone in the Flagship simulation, corresponding to an area of $\sim 2758 \text{ deg}^2$ and a sky fraction of $f_{\text{sky}} = 0.067$.

We only select objects with a signal-to-noise ratio (S/N) ≥ 5 – where S/N is defined as the ratio of the flux over the flux uncertainty in the I_E band – and with the NNPZ flag equal to zero, indicating no issues with the computed photo- z s. The lens sample is further selected with a magnitude cut in the I_E band of $I_E \leq 23.5$ – including the continuum flux, emission lines as described in model 3 of Pozzetti et al. (2016), internal attenuation, and Milky Way extinction. We do not apply a direct magnitude cut to the source sample, which results in a very large catalogue. Therefore, to speed up the computation time, we reduce the source catalogue by removing objects based on their shear weights. However, Flagship does not incorporate shear weights yet, which depend on the shape measurement algorithm and require image simulations. Instead, we approximate the shear weights as a function of the S/N by fitting a simple functional form that follows the `lensfit` (Miller et al. 2007, 2013) shear weights from the public KiDS-1000 catalogue (Giblin et al. 2021),

$$w(\text{SNR}) = \frac{1}{1 + \left(\frac{10}{\text{S/N}}\right)^{2.5}}. \quad (26)$$

Then, we only keep objects with weights larger than uniform random draws, which preferentially removes low S/N objects, preserves the $n(z)$, and minimises the shape noise.

Both source and lens samples are further restricted with a cut in the photo- z (z_b) range $0.2 < z_b < 2.5$, and each sample is divided into 6 equipopulated tomographic redshift bins. The resulting shape noise is $\sigma_e \sim 0.37$ (with σ_e the total shape disperion), and the number densities of sources and lenses are ~ 5.99 and ~ 1.69 galaxies/arcmin 2 , respectively, in each tomographic bin. Figure 2 shows the resulting $n(z_s)$ distribution of

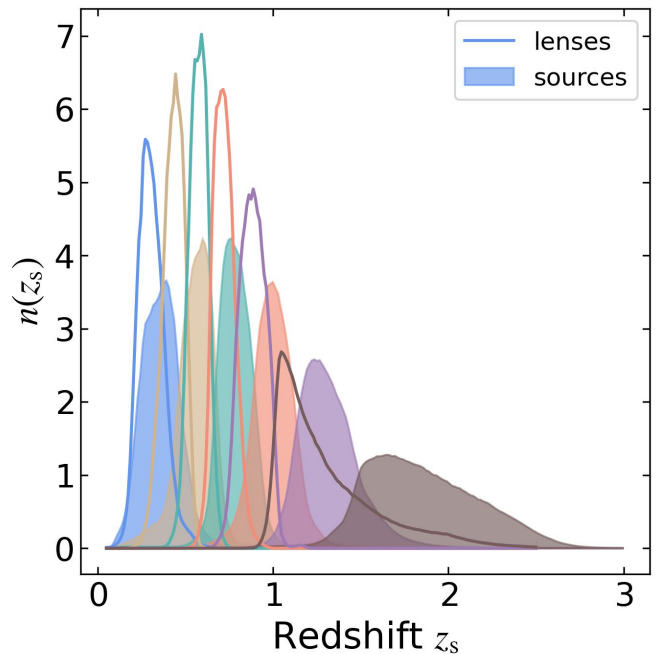


Fig. 2. Normalised true redshift distribution, z_s , of sources and lenses for the galaxy samples defined in Sect. 4.2.

both sources and lenses, with z_s the true redshift values. We note that, although we consider these samples as *Euclid* DR1, the final samples that will be used in the cosmology analyses are still subject to change.

4.3. Measurement of IA values in Flagship

Here, we derive the IA parameters that best describe the samples defined in the previous section. First, we measure the WL, GC, and GGL C_ℓ using the `Heracles` (Euclid Collaboration: Tessore et al. 2025) code.⁸ This code allows us to measure angular power spectra by employing discrete data sets, obtained at the galaxies' positions. The key ingredients that `Heracles` needs to compute the angular power spectra are the galaxy positions, the galaxy shears (and their intrinsic ellipticities and shear weights), the visibility map, and the $n(z)$ distribution of sources and lenses. The C_ℓ that `Heracles` outputs are convolved with the visibility map, so that they have an amplitude proportional to the area covered by the 30 deg cone in our case, while also accounting for its mask. This complicates the computation of the covariance matrix (Sect. 3.3), because it also needs to be convolved with the mask. To avoid this, we choose to deconvolve the measured C_ℓ by dividing their associated correlation function by the correlation function of the mask, and transforming back to harmonic space (Ruiz-Zapatero et al. in preparation). This approach is similar to the `PolSpice` methodology (Challinor et al. 2011), with the crucial difference that spin-2 fields are transformed with their associated Wigner matrices, as opposed to the opposite spin matrix (as described in Schneider et al. 2002; Chon et al. 2004; Camphuis et al. 2022). To make the correlation function of the mask invertible, we multiply it with a logistic function. This is equivalent to throwing away scales in singular value decomposition algorithms. Nevertheless, we observe that performing this regularisation in configuration space performs better than doing so in harmonic space.

⁸ <https://heracles.readthedocs.io/stable/index.html>

Once the C_ℓ are computed, we determine the IA values by sampling over A_1 , A_2 , η_1 , η_2 , and $A_{1\delta}$. We consider the flat priors $A_1 = [0, 3]$, $A_2 = [-2, 2]$, $\eta_1 = [0, 4]$, $\eta_2 = [-4, 4]$, and $A_{1\delta} = [-2, 3]$ based on the results from P26. We fix the cosmological and other nuisance parameters to their fiducial values (Table 3). We perform this analysis with CosmoSIS, following the implementation described in Sect. 3. In particular, for this analysis, we use the EuclidEmulator2 to obtain the nonlinear matter power spectrum, since it accurately describes the measurements performed in Flagship. Figure 3 shows the constraints on the IA values for both the z NLA and z TATT models when considering a scale cut of $k_{\max} = 3 h \text{ Mpc}^{-1}$ in the WL C_ℓ and of $k_{\max} = 0.3 h \text{ Mpc}^{-1}$ in the GGL and GC C_ℓ . We can see different posterior distributions for A_1 and η_1 between both IA models, which are explained by the fact that the higher-order z TATT terms capture additional information, particularly at small scales, while the z NLA model tries to describe the Flagship DVs by shifting the A_1 and η_1 values. We show the comparison between the measured C_ℓ in Flagship and the z NLA and z TATT theory predictions, based on the constraints of Fig. 3, in Appendix A. There, we can see that z TATT describes the Flagship DV better, with maximum differences of 2σ between both. For this reason, and also because we need all z TATT terms to generate different modelling scenarios in our results (see Table 2), we will employ the maximum of the posterior distribution of the z TATT constraints from Fig. 3 as IA fiducial values, which are specified in Table 3.

Finally, we are interested in understanding how the IA parameter constraints from P26 compare to those derived in this work. P26 also employed the Flagship simulation, although the authors used a slightly different galaxy sample selection and a different estimator to compute the IA signal. We show this comparison in Appendix B and confirm the agreement between both cases. Additionally, for our fiducial sample definition, we show the level of overlap in the z TATT constraints when removing the last redshift bins. This is an important test since P26 found that the IA implementation in Flagship deviates from a power-law dependence at high redshift. Even though we find good agreement with the z TATT constraints for both scenarios, which indicates that the constraints in Fig. 3 are valid, we should be cautious in future works with real data about the redshift dependence of IA.

4.4. Generation of synthetic DVs

We generate synthetic noiseless DVs using the fiducial values described in Table 3 and the pipeline described in Sect. 3. We use an $f_{\text{sky}} = 0.067$, as described in Sect. 4.2, and the $n(z)$ for sources and lenses. As for the IA parameters, we use the fiducial values computed with the z TATT model in Sect. 4.3. We generate two synthetic DVs from the z TATT constraints: one generated with z NLA (fixing $A_2 = \eta_2 = A_{1\delta} = 0$) and the other with z TATT.

5. Results

In this section, we present the main results for the different IA models considered in this analysis. First, we analyse how the constraining power changes as a function of different analysis choices. Second, we analyse the bias in both IA and cosmological parameters that arise from mismodelling IA. Finally, we focus on analysing the degeneracies between IA and photo- z nuisance parameters.

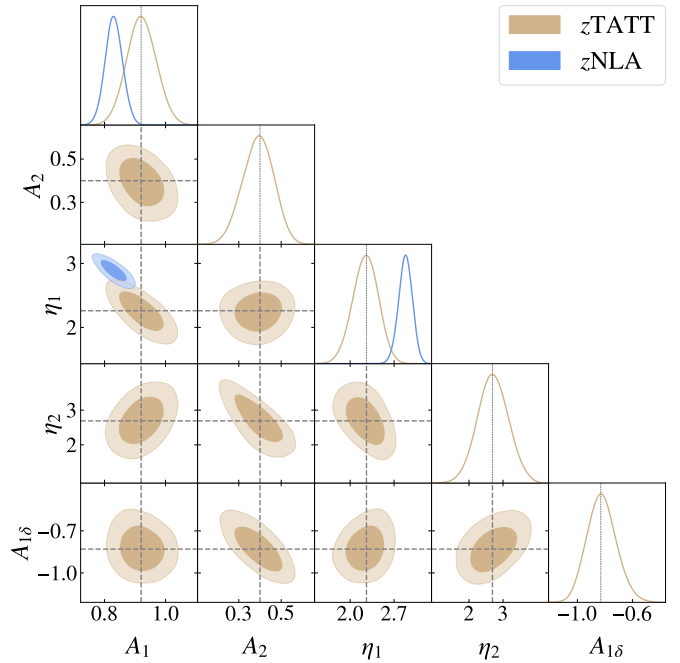


Fig. 3. IA constraints for the measured Flagship C_ℓ described in Sect. 4.3 when using the z TATT (tan) and the z NLA (blue) IA models. The dashed lines correspond to the maximum of the posterior distributions of the z TATT parameters, which are used to generate the synthetic DVs in Sect. 4.4.

5.1. Constraining power

Here we study how the constraining power on cosmological parameters depends on the IA model (z NLA vs. z TATT) used to generate the synthetic DVs (Sect. 4.3), together with other analysis choices, such as scale cuts (defined in Sect. 3.4), cosmological probe combinations (3×2 pt, 2×2 pt, and WL), the assumed cosmological model (Λ CDM vs. $w_0 w_a$ CDM), and IA priors. A summary of the resulting constraining power for the different cases is presented in Table 4, in terms of the 68% percentiles in the IA and cosmological parameters.

5.1.1. IA modelling and scale cuts

Figure 4 shows the IA (left) and cosmological (right) parameter constraints for four scenarios of 3×2 pt analyses: z NLA (blue) and z TATT (tan), with a scale cut of $k_{\max} = 1 h \text{ Mpc}^{-1}$ (unfilled) and $k_{\max} = 3 h \text{ Mpc}^{-1}$ (filled) for the WL C_ℓ . We analyse the change in constraining power from two perspectives: i) fixing the scale cuts and varying the IA model and ii) fixing the IA model and varying the scale cuts.

The first case shows that z NLA yields slightly tighter constraints in A_1 and η_1 than z TATT (a factor of ~ 1.25 in A_1 and ~ 1.1 in η_1 , based on Table 4), since the former has fewer parameters. However, this does not translate into tighter constraints in the cosmological parameters, with z NLA and z TATT yielding similar constraining power. This allows us to use a more flexible IA model (with more parameters) without losing constraining power.

The second case indicates that the constraining power in the IA parameters increases for both z NLA and z TATT with the inclusion of smaller scales. This is especially true for z TATT, which presents bimodalities in the posterior distributions of its higher-order terms (A_2 , η_2 , and $A_{1\delta}$) at $k_{\max} = 1 h \text{ Mpc}^{-1}$, but

Table 4. 68% percentile of the IA and cosmological parameters for different IA models, scale cuts, cosmological probes, cosmological model (Λ CDM versus w_0w_a CDM), and IA priors.

Case	A_1	A_2	η_1	η_2	$A_{1\delta}$	Ω_m	S_8	w_0	w_a
Λ CDM z NLA $k_{\max} = 1 \text{ h Mpc}^{-1}$ 3×2 pt	0.063	-	0.277	-	-	0.019	0.010	-	-
Λ CDM z TATT $k_{\max} = 1 \text{ h Mpc}^{-1}$ 3×2 pt	0.079	0.380	0.301	2.184	0.584	0.020	0.010	-	-
Λ CDM z NLA $k_{\max} = 3 \text{ h Mpc}^{-1}$ 3×2 pt	0.054	-	0.234	-	-	0.017	0.009	-	-
Λ CDM z TATT $k_{\max} = 3 \text{ h Mpc}^{-1}$ 3×2 pt	0.067	0.111	0.268	0.673	0.197	0.017	0.009	-	-
Λ CDM z NLA $k_{\max} = 3 \text{ h Mpc}^{-1}$ 2×2 pt	0.094	-	0.546	-	-	0.022	0.014	-	-
Λ CDM z TATT $k_{\max} = 3 \text{ h Mpc}^{-1}$ 2×2 pt	0.118	0.659	0.596	2.505	1.002	0.022	0.014	-	-
Λ CDM z NLA $k_{\max} = 3 \text{ h Mpc}^{-1}$ WL	0.069	-	0.280	-	-	0.025	0.010	-	-
Λ CDM z TATT $k_{\max} = 3 \text{ h Mpc}^{-1}$ WL	0.118	0.202	0.337	0.939	0.357	0.025	0.010	-	-
w_0w_a CDM z NLA $k_{\max} = 3 \text{ h Mpc}^{-1}$ 3×2 pt	0.116	-	0.248	-	-	0.038	0.022	0.357	0.946
w_0w_a CDM z TATT $k_{\max} = 3 \text{ h Mpc}^{-1}$ 3×2 pt	0.131	0.138	0.273	0.651	0.215	0.04	0.022	0.370	0.951
Λ CDM z NLA $k_{\max} = 3 \text{ h Mpc}^{-1}$ narrow IA prior 1	0.054	-	0.226	-	-	0.017	0.009	-	-
Λ CDM z TATT $k_{\max} = 3 \text{ h Mpc}^{-1}$ narrow IA prior 1	0.066	0.110	0.265	0.670	0.194	0.017	0.009	-	-
Λ CDM z NLA $k_{\max} = 3 \text{ h Mpc}^{-1}$ narrow IA prior 2	0.047	-	0.152	-	-	0.016	0.009	-	-
Λ CDM z TATT $k_{\max} = 3 \text{ h Mpc}^{-1}$ narrow IA prior 2	0.055	0.069	0.151	0.261	0.156	0.017	0.009	-	-

not at $k_{\max} = 3 \text{ h Mpc}^{-1}$, where there is a factor of ~ 3 increase in the constraining power. Such a result is expected because the higher-order terms are mainly constrained by small scales. This can be better seen in Fig. 5, where we show the cross-correlation of source redshift bin 1⁹ with the rest of the redshift bins for the WL C_ℓ – which is the probe where the scale cuts are varied – for both the z NLA (blue) and z TATT (tan) IA models. The vertical lines show the scale cuts, in terms of ℓ_{\max} , which correspond to $k_{\max} = 1 \text{ h Mpc}^{-1}$ (dashed line) and $k_{\max} = 3 \text{ h Mpc}^{-1}$ (solid line).¹⁰ The poor constraints on A_2 , η_2 , and $A_{1\delta}$ for z TATT at $k_{\max} = 1 \text{ h Mpc}^{-1}$ arise because the z TATT signal is very similar to the z NLA one up to that scale cut. As a result, the higher-order terms in z TATT are not well constrained unless smaller scales are included. Motivated by the greater impact of baryonic effects when including smaller scales, we also checked if there were degeneracies between the IA parameters and T_{AGN} , but did not find any. Regarding the constraining power of the cosmological parameters in Fig. 4, it increases when changing the scale cuts, in a similar way to the constraints of A_1 and η_1 .

5.1.2. Combination of cosmological probes

Figure 6 shows the constraining power on the cosmological parameters S_8 and Ω_m for different combinations of cosmological probes: 3×2 pt, 2×2 pt (GGL and GC), and WL. We show the constraints for z NLA (filled contours) and z TATT (unfilled contours) for a fixed scale cut of $k_{\max} = 3 \text{ h Mpc}^{-1}$ in the WL C_ℓ . As expected, the most constraining case is 3×2 pt, since it combines all three probes. Similar to Fig. 4, we observe virtually the same constraining power in S_8 and Ω_m when employing z NLA and z TATT, for both 2×2 pt and WL-only cases.

Table 4 indicates that the z NLA parameters are better constrained in the 3×2 pt and WL cases, compared to 2×2 pt, since the main constraining probe for IA is WL, due to the inclusion of smaller scales. That is also the case for z TATT, except from the A_1 constraints, which are similar for 2×2 pt and WL.

⁹ We only include the source redshift bin 1 in this comparison since it is the bin that presents the largest difference between z NLA and z TATT.

¹⁰ Note that the scale cuts defined for z NLA and z TATT may differ (blue for z NLA and tan for z TATT), given that the IA signal is also taken into account when computing the scale cuts (Eq. 25).

We include in Appendix C a similar analysis to that performed in Figs. 4 and 6, but only sampling over the cosmological parameters ($\Omega_m h^2$, h , and $A_s \times 10^9$) and the IA parameters, while fixing all other parameters. This is important because other nuisance parameters can interfere with IA when studying the constraining power. Thus, if we do not find any differences in the constraining power of z NLA and z TATT in the best-case scenario, which would be to know the true value of all the other nuisance parameters, we will not find them in a less constraining scenario. To summarise, although fixing the remaining nuisance parameters improves the overall constraining power, Appendix C shows that the relative constraining power of z NLA and z TATT remains essentially the same.

5.1.3. Cosmological model

Table 4 includes constraints when considering a w_0w_a CDM model at $k_{\max} = 3 \text{ h Mpc}^{-1}$. We study the change in constraining power from also two perspectives: i) varying the IA model in w_0w_a CDM and ii) comparing the w_0w_a CDM and Λ CDM models for a given IA model. The first case is very similar to what we saw for the Λ CDM model, with the IA parameters being a ~ 1.1 factor better constrained in z NLA than in z TATT and the cosmological parameters being virtually unaffected. The second case shows that the overall constraining power in the IA and the cosmological parameters decreases for the w_0w_a CDM model, with A_1 and A_2 being a factor ~ 2.2 and ~ 1.2 less constrained, respectively, and the cosmological parameters, Ω_m and S_8 , being a factor ~ 2.4 less constrained.

5.1.4. IA priors

We study the case of considering more stringent priors on the IA parameters to understand if we lose constraining power with the IA priors defined for the fiducial analysis. In this way, we test the importance of knowing a priori the allowed range of the IA parameters. We consider two scenarios:

- narrow IA prior 1: $A_1 \in [0.5, 1.5]$, $A_2 \in [-0.5, 1]$, $A_{1\delta} \in [-3, 1]$, $\eta_1 \in [1, 3.5]$, $\eta_2 \in [0, 6]$,
- narrow IA prior 2: $A_1 \in [0.7, 1.1]$, $A_2 \in [0.2, 0.6]$, $A_{1\delta} \in [-1.2, -0.4]$, $\eta_1 \in [2, 2.5]$, $\eta_2 \in [2.2, 3]$.

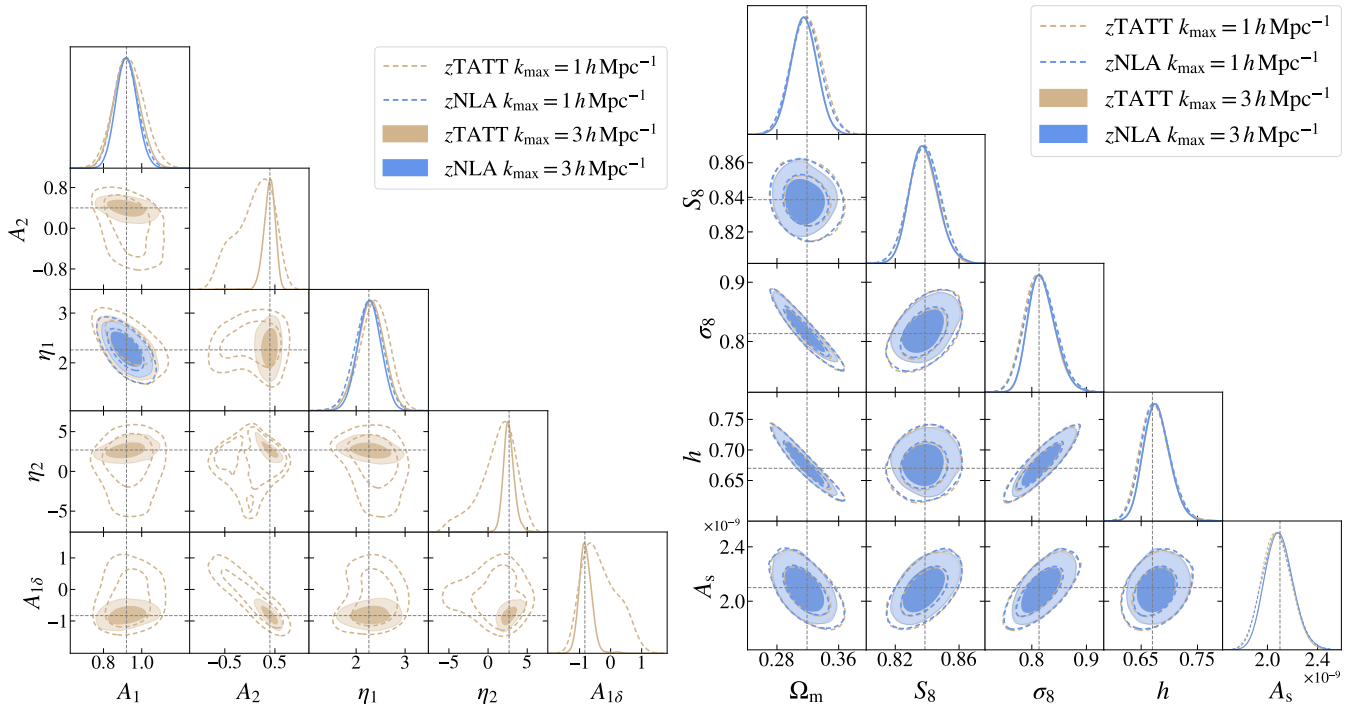


Fig. 4. IA (left) and cosmological parameters (right) constraints for $z\text{NLA}$ (blue) and $z\text{TATT}$ (tan) at different scale cuts in the WL C_ℓ , $k_{\text{max}} = 1 \text{ hMpc}^{-1}$ (unfilled) and $k_{\text{max}} = 3 \text{ hMpc}^{-1}$ (filled). The dashed lines indicate the fiducial values of the parameters. The tan contours on the right plot are not well distinguished because they overlap with the blue ones.

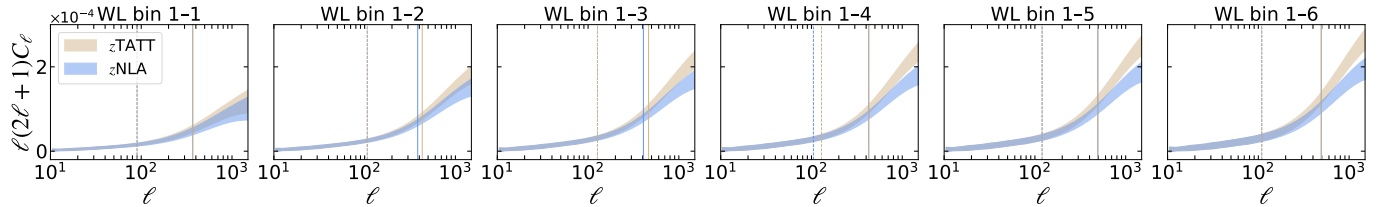


Fig. 5. Comparison of the $z\text{NLA}$ (blue) and $z\text{TATT}$ (tan) WL C_ℓ for the cross-correlation of the source redshift bin 1 with the other bins. Vertical lines show the scale cuts applied to the analysis for $k_{\text{max}} = 1 \text{ hMpc}^{-1}$ (dashed line) and $k_{\text{max}} = 3 \text{ hMpc}^{-1}$ (solid line) in the WL $C(\ell)$ s.

Although Table 4 indicates that the constraining power in the IA parameters slightly increases, especially for the second set of narrow IA priors, where the prior boundaries of the IA parameters are hit, the constraints on the cosmological parameters for both sets of narrow priors are virtually the same as the ones obtained from the fiducial analysis. This indicates that, for the setup considered in this work, the choice of the IA priors is not that critical. However, studies of direct constraints on IA are still necessary, both because future *Euclid* data releases will decrease statistical uncertainties, and to constraint IA evolution with redshift.

5.2. Mismodelling of IA

Since the “true” model describing IA is unknown, we need to evaluate by how much we can bias our cosmological analysis if we use an IA model different from that describing the data. For that, we employ the DVs described in Sect. 4.4, one generated with $z\text{NLA}$ and the other with $z\text{TATT}$, and model them with the six IA models described in Sect. 2.2: NLA, $z\text{NLA}$, TATT, $z\text{TATT}$, $k\text{NLA}$, and $z\text{TATT-}b_1$. Here, we assume $k_{\text{max}} = 3 \text{ h Mpc}^{-1}$ for the WL C_ℓ , given that using $k_{\text{max}} = 1 \text{ h Mpc}^{-1}$ does not constrain well the higher-order $z\text{TATT}$ parameters (as seen in Fig. 4). As a result, analyses limited to $k_{\text{max}} = 1 \text{ h Mpc}^{-1}$

could suffer from exacerbated biases in the IA and cosmological parameters.

Before performing any analysis, we can gain some intuition on which cases are more prone to biases. On the one hand, we expect a low bias when employing the DV generated with $z\text{NLA}$ and model it with either $z\text{TATT}$ or $k\text{NLA}$, since $z\text{NLA}$ constitutes a subspace of these models. However, it is still interesting to study the cases where the modelling is done with redshift-independent models, such as NLA and TATT, or by fixing $A_{1\delta} = 1$, as in the case of $z\text{TATT-}b_1$. On the other hand, when employing a synthetic DV generated with $z\text{TATT}$, the use of NLA-like models (NLA, $z\text{NLA}$, and $k\text{NLA}$) will miss the $z\text{TATT}$ higher-order terms. Moreover, using a redshift-independent TATT model or $z\text{TATT-}b_1$ will also miss some of the dependencies of the $z\text{TATT}$ synthetic DV. As a consequence, the mismodelling of the synthetic DV generated with $z\text{TATT}$ is more prone to biases in both IA and cosmological parameters.

Figure 7 shows the constrained IA parameters when mismodelling the $z\text{NLA}$ (left) and the $z\text{TATT}$ (right) synthetic DVs. As a reference, we show that the fiducial values are recovered when the model used to generate and analyse IA coincides, depicted as black (left) and tan (right) unfilled contours. The plot on the left shows that the fiducial values of the $z\text{NLA}$ DV are also recovered with both $z\text{TATT}$ and $k\text{NLA}$, as expected, with their higher-order

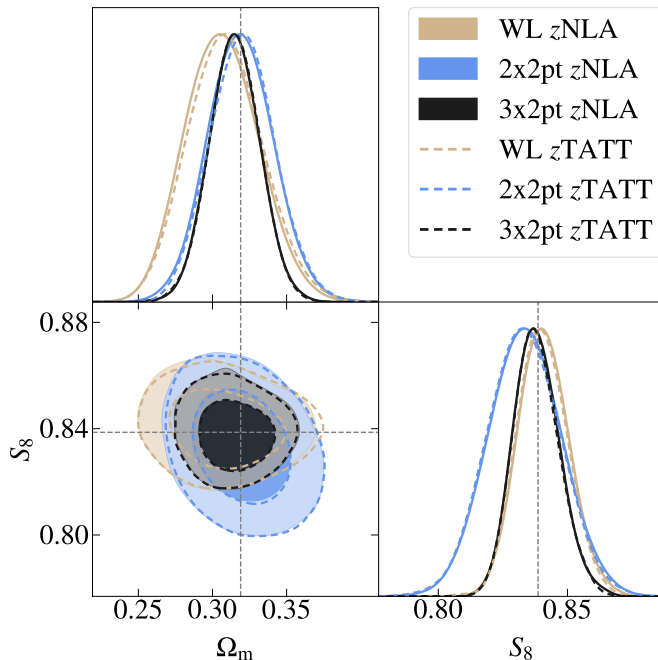


Fig. 6. Constraints on S_8 and Ω_m for z NLA (filled contours) and z TATT (unfilled contours), and for different combinations of cosmological probes: WL (tan), 2×2 pt (blue), and 3×2 pt (black). The dashed lines indicate the fiducial values of the parameters.

terms centred on 0. However, the redshift-independent models (NLA and TATT) show a significant bias in A_1 , while z TATT- b_1 exhibits non-negligible biases in both A_1 and A_2 . The plot on the right shows that none of the IA models, except for z TATT, are able to recover the fiducial IA parameters describing the synthetic DV. However, the biases are different depending on the assumed IA model, with z NLA and k NLA describing the DV better, since they include the two first-order z TATT terms, A_1 and η_1 . As for the redshift-independent models, NLA and TATT, they both have significant biases in A_1 , although TATT is able to recover the fiducial values of both A_2 and $A_{1\delta}$. Finally, it is interesting to note that z TATT- b_1 , even though it samples 4/5 parameters from z TATT, shows a large bias in all of its four parameters. This is because the assumption $A_{1\delta} = 1$ is not satisfied in the Flagship DVs, as seen in Fig. 3. Interestingly, the assumption of $A_{1\delta} > 0$ is not satisfied in other studies either, such as the MASSIVE-BLACK II hydrodynamical simulation (Di Matteo et al. 2012; Khandai et al. 2015) at high redshifts (Samuroff et al. 2021), the DESY3 redMaGiC low- z sample (Samuroff et al. 2023), and the analysis from P26. Although we do not show here the results for the w_0w_a CDM scenario, for conciseness, the biases are very similar, albeit with broader contours in the IA parameters.

In Fig. 8, we study the effect of mismodelling IA in the cosmological parameters S_8 , Ω_m , w_0 , and w_a , to which 3×2 pt analyses are most sensitive. We assess the mismodelling effect by defining two metrics: i) bias in the 2D parameter planes of S_8 – Ω_m and w_0 – w_a , computed as the distance between the peaks of the marginalised posteriors, in terms of $n\sigma$; and ii) $\Delta\chi^2_v$, defined as the difference between the $\chi^2_v := \chi^2/v$ (with v the degrees of freedom) of the mismodelled and correctly modelled analyses, where each χ^2 is evaluated from the maximum χ^2 posterior distribution of each chain. Moreover, we compute the $\Delta\chi^2_v$ value that corresponds to a probability to exceed (PTE) of 2%, which is $\Delta\chi^2_v \sim 0.08$. This quantity captures how unlikely it is to find

a $\Delta\chi^2_v$ larger than that given by a PTE value. That is, it marks a region of very unlikely large $\Delta\chi^2_v$, which may be produced by mismodelling effects. Following previous works (Krause et al. 2021; Campos et al. 2023; Leonard et al. 2024), we define 0.3σ as the limit at which an IA model is introducing a significant bias.

The cosmological bias can be computed in two different ways: bias with respect to the fiducial values or relative to the results of an analysis without IA mismodelling. Given that the correctly modelled chain can still deviate from the fiducial values, due to factors such as projection effects or constraining power, we compute the bias with respect to the correctly modelled chain. This ensures that the estimated $n\sigma$ differences only reflect the impact of the different IA models.

The plots in Fig. 8, which show the bias versus the $\Delta\chi^2_v$, are useful to understand which cases can be problematic for a successful analysis. If the $\Delta\chi^2_v$ and the bias increase at the same time (tan shaded area), this indicates that a difference between the DV and the model implies a bias in cosmology, and this can be detected from a large $\Delta\chi^2_v$ in the analysis. A low bias and a high $\Delta\chi^2_v$ (blue shaded area) implies that the residuals introduced by IA mismodelling project only weakly onto the directions spanned by the cosmological parameters, producing a large mismatch between the DV and the theoretical description, but only a small cosmological bias. Conversely, low values of both quantities (green shaded area), in the case where the fiducial IA parameters in Fig. 7 were not recovered, indicate that the model is flexible enough to absorb the differences in their parameter space. The problematic scenario occurs when the $\Delta\chi^2_v$ is low, but the bias is high (red shaded area). In these cases, the residual IA differences are absorbed by a shift in cosmology, and the issue cannot be detected by studying the $\Delta\chi^2_v$ alone in real-data analyses.

The plot on the left of Fig. 8 shows the bias in the S_8 – Ω_m plane as a function of $\Delta\chi^2_v$ for the cases where the DV is generated with z NLA (triangle) or with z TATT (circles) and for the Λ CDM (empty symbols) and w_0w_a (filled symbols) cases. The different colours depict the IA model used to analyse the DV. Most of the points with a bias larger than 0.3σ are from w_0w_a cases and correspond to points generated with z TATT. Only two points, which correspond to the z TATT w_0w_a CDM case modelled with TATT and NLA, have a high $\Delta\chi^2_v$ and a large bias in S_8 – Ω_m . However, there are six cases that present a low $\Delta\chi^2_v$, but a large bias, three of them modelled with z TATT- b_1 . Meanwhile, two other cases have a large $\Delta\chi^2_v$ but a low bias, and correspond to the Λ CDM cases of the points with large $\Delta\chi^2_v$ and large bias. The plot on the right shows the bias in the w_0 – w_a plane versus $\Delta\chi^2_v$. The two previous cases of z TATT w_0w_a CDM case modelled with TATT and NLA also show correlation with $\Delta\chi^2_v$ and bias in the w_0w_a plane. Now, there are four cases with low $\Delta\chi^2_v$ and high bias. As a summary, all the models, except from z TATT, which always covers the truth in the z NLA and z TATT DVs, can potentially bias cosmological parameter estimation.

5.3. Degeneracies of IA with photometric redshifts

The degeneracies between photo- z and IA parameters (Li et al. 2021; Fischbacher et al. 2023; Leonard et al. 2024; Mill et al. 2025), if not properly considered, can lead to misinterpretations of the effects that IA can have on cosmological analyses. In particular, a poor estimation of photo- zs might lead to biased IA constraints and, consequently, to biased cosmological constraints.

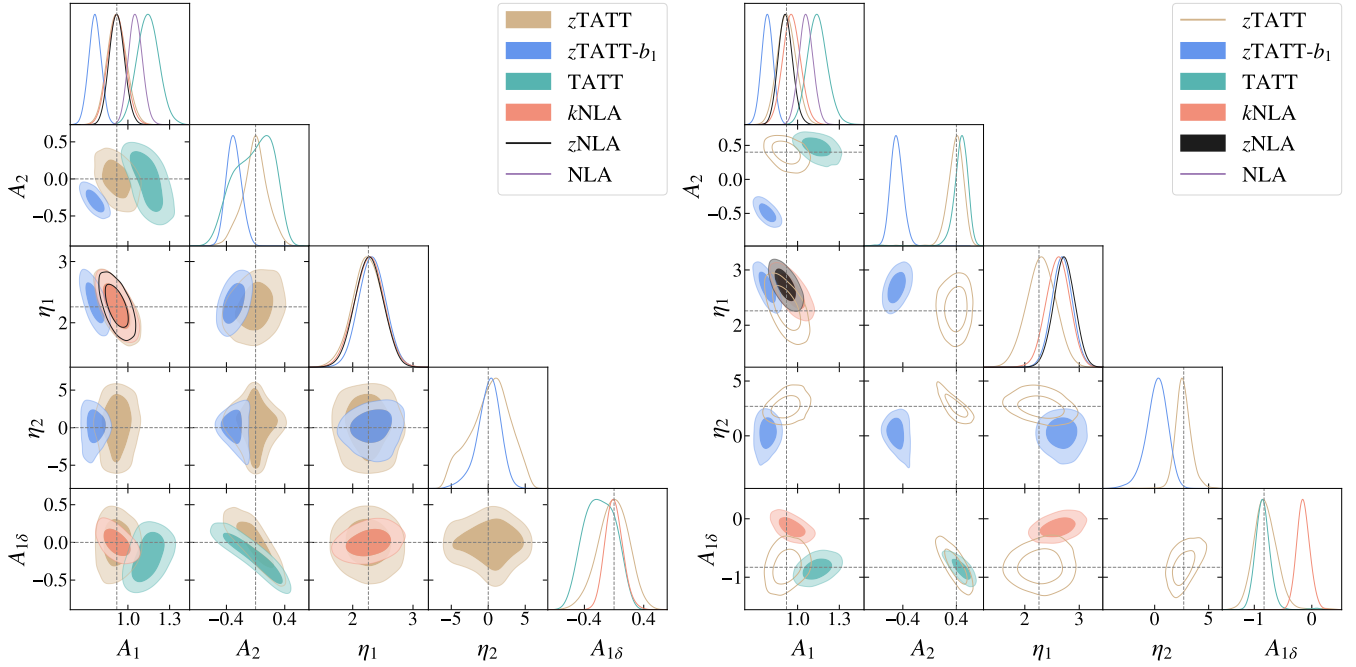


Fig. 7. IA parameter constraints when mismodelling synthetic DVs generated with $zNLA$ (left) or with $zTATT$ (right) with all possible IA models presented in Sect. 2.2, and for the Λ CDM model. The case where the IA model is the same as the one used to generate the synthetic DV is depicted as black (left) or tan (right) unfilled contours. The dashed lines indicate the fiducial values of the parameters.

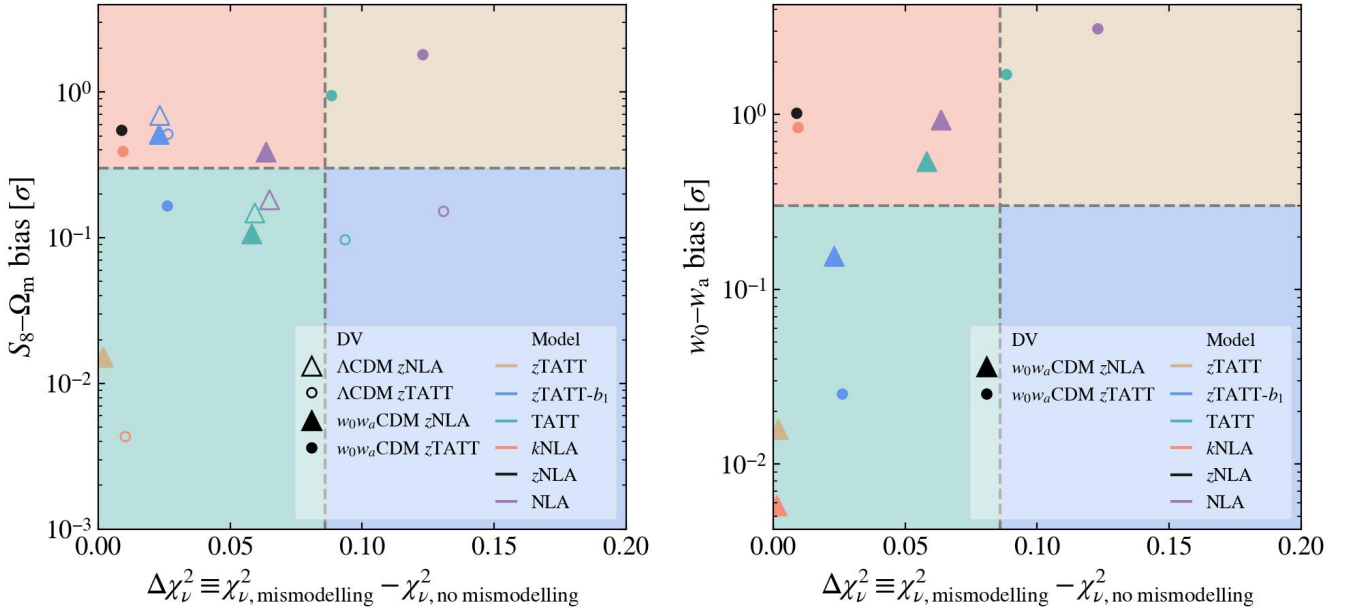


Fig. 8. Bias in the $S_8 - \Omega_m$ plane (left) and the $w_0 - w_a$ plane (right) versus the $\Delta\chi^2_\nu$, defined as the difference between the χ^2_ν when performing mismodelling and when employing the same IA model that was used to generate the DV. The horizontal line depicts a 0.3σ bias, while the vertical line depicts the $\Delta\chi^2_\nu$ value that corresponds to a probability to exceed of 2%. The shaded colour areas indicate the different regimes in relation with the level of cosmological bias and $\Delta\chi^2_\nu$.

We inspect these degeneracies in Fig. 9, which shows the constraints of the IA parameters (and of w_0 and w_a for some cases) versus the source photo- z parameters for $zNLA$ (blue) and $zTATT$ (tan) at $k_{\max} = 3 \text{ h Mpc}^{-1}$ for the WL C_ℓ . We consider the case of a Λ CDM (unfilled contours) and a w_0w_a CDM (filled contours) scenario. Generally, we do not find significant degeneracies between IA and photo- z parameters, for either Λ CDM or w_0w_a CDM models. However, a mild degeneracy appears between the Δz_s parameter of bin 6 and the η_1 IA parameter, es-

pecially for w_0w_a CDM. For the higher-order $zTATT$ terms, we do not find degeneracies with Δz_s . In order to understand why this analysis does not show the degeneracies from previous literature, we tested wider priors in Δz_s , defined as flat priors with a 3σ width of those defined in Table 3. Although not shown here for conciseness, we reran all the cases of Fig. 9 with these wider priors, and observed strong degeneracies between A_1 and all redshift bins Δz_s , η_1 and redshift bin 6, and $A_{1\delta}$ and the first five redshift bins for Λ CDM. This implies that if the photo- z

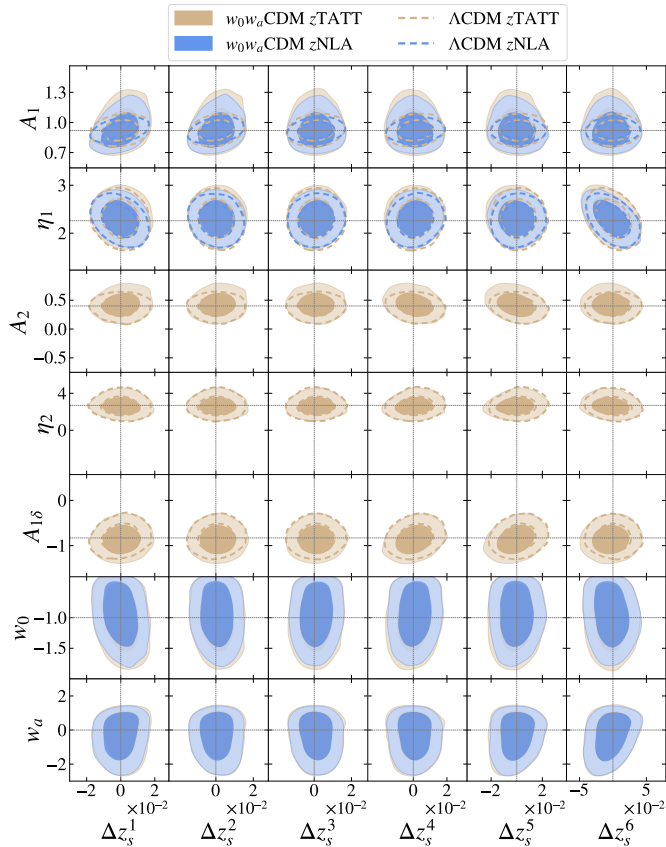


Fig. 9. Degeneracies between IA, w_0 , w_a , and Δz_s parameters for z TATT (tan) and z NLA (blue), and for w_0w_a CDM (filled contours) and Λ CDM (unfilled contours). The dashed lines indicate the fiducial values of the parameters.

Gaussian priors are not correctly centred, the inferred IA parameters from WL analyses will be biased. These effects can be revealed through, for example, colour-based split consistency tests, as shown in Li et al. (2021). As in the case with the fiducial Gaussian priors, the higher-order z TATT terms do not present degeneracies with Δz_s . Thus, if the photo- z s have at least the level of precision of stage-III surveys, and are correctly centred, we will not be affected by strong degeneracies between IA and photo- z s.

Finally, we also tested if there were other degeneracies between IA and other nuisance parameters – such as galaxy bias, magnification, and multiplicative shear bias – but did not find any.

6. Conclusions

Euclid will deliver a powerful survey that will observe billions of galaxies and constrain cosmological parameters with unprecedented precision. However, to achieve this, all systematic effects also need to be quantified and corrected at an unprecedented level. Amongst the sources of systematic effects that will affect *Euclid*, we focused on the IA of galaxies, since they are a major contaminant to the WL and GGL observables, and can bias the estimation of cosmological parameters.

Our main goal was to assess which of the IA models currently used in stage-III survey analyses, NLA and TATT, is preferred to describe IA for *Euclid* DR1 analyses. We defined six tomographic redshift bins for sources and lenses, in an area of $\sim 2500 \text{ deg}^2$, including systematic effects from IA, magnifica-

tion, galaxy bias, multiplicative shear bias, and photo- z uncertainties. Given that a comparison between the NLA and TATT models (and variations of them) depends on the assumed IA central values, we employed the Flagship simulation to estimate these values for our *Euclid* DR1 sample. These IA values were used to generate synthetic DVs, with which we performed 3×2 pt analyses to constrain the cosmological and IA parameters.

We determine the best IA modelling choice for *Euclid* DR1 by considering three approaches:

- **Constraining power:** we compared the constraining power when using NLA and TATT as a function of different analysis choices, such as scale cuts, combination of cosmological probes, cosmological model (Λ CDM versus w_0w_a CDM), and IA priors. Since NLA is a subspace of TATT, we expect to have more constraining power with the former due to its fewer parameters. This will be true if no extra information comes from the higher-order TATT terms at small scales. As a function of scale cuts, when setting $k_{\max} = 1 \text{ h Mpc}^{-1}$ for the WL C_ℓ , the higher-order TATT terms are unconstrained. However, if we set $k_{\max} = 3 \text{ h Mpc}^{-1}$ these terms are constrained and the loss of constraining power with respect to NLA is virtually null. As a result, if we include scales small enough we can expect NLA and TATT to yield very similar constraining power for a 3×2 pt Λ CDM analysis. This is also true for a 2×2 pt and a WL-only scenario, as well as for the w_0w_a CDM case. Finally, we tested that the constraining power does not change when reducing the width of the IA priors.
- **IA mismodelling:** we analysed the cosmological bias caused by mismodelling IA, that is, modelling IA with a different model than that of the DV. We studied the mismodelling effect for two DVs: one generated with NLA and one generated with TATT. We find that the only IA model able to avoid cosmological bias is the TATT model with redshift dependence (z TATT), given that it is the more general model to cover the synthetic DVs. Importantly, we find that modelling IA without redshift dependence, or fixing the $A_{1\delta} = 1$, can induce significant cosmological biases.
- **Degeneracy between IA and photo- z parameters:** we do not find significant degeneracies between IA and photo- z parameters when assuming a Gaussian prior, with a similar width of stage-III surveys, on the photo- z nuisance parameters. However, stronger degeneracies appear when employing a flat prior with a width 3 times the standard deviation of the Gaussian priors. Thus, if the photo- z uncertainties for *Euclid* DR1 are kept at least at the same level of precision as in stage-III surveys, we will not suffer from degeneracies between IA and photo- z s. It is important to note that we do not find degeneracies with the higher-order TATT terms, A_2 and η_2 , for any of the prior choices, which indicates that TATT is as reliable as NLA in this regard.

The combination of the lessons learnt from these approaches suggests that the preferred IA model to analyse *Euclid* DR1 data is z TATT, assuming the redshift-dependence is correctly captured with a power-law, given that it does not reduce the constraining power, it is the most robust one regarding the mismodelling of IA, and it does not present degeneracies with photo- z s. We leave for future work a full analysis that employs the Flagship simulation measurements as DVs, instead of synthetic DVs, together with other IA models not considered in this work.

Acknowledgements. The authors would like to thank Aniruddh Herle and Casper Verder for useful comments on this work. DNG and H. Hoekstra acknowledge support from the European Research Council (ERC) under the European Union's

Horizon 2020 research and innovation program with Grant agreement No. 101053992. It has been supported by the Ramon y Cajal fellowship (RYC2023-045531-I) funded by the State Research Agency of the Spanish Ministerio de Ciencia, Innovación y Universidades, MICIU/AEI/10.13039/501100011033/, and Social European Funds plus (FSE+). It also acknowledges support from the same ministry, via projects PID2019-11317GB, PID2022-141079NB, PID2022-138896NB; the European Research Executive Agency HORIZON-MSCA-2021-SE-01 Research and Innovation programme under the Marie Skłodowska-Curie grant agreement number 101086388 (LACEGAL) and the programme Unidad de Excelencia María de Maeztu, project CEX2020-001058-M. The Euclid Consortium acknowledges the European Space Agency and a number of agencies and institutes that have supported the development of *Euclid*, in particular the Agenzia Spaziale Italiana, the Austrian Forschungsförderungsgesellschaft funded through BMIMI, the Belgian Science Policy, the Canadian Euclid Consortium, the Deutsches Zentrum für Luft- und Raumfahrt, the DTU Space and the Niels Bohr Institute in Denmark, the French Centre National d'Etudes Spatiales, the Fundação para a Ciência e a Tecnologia, the Hungarian Academy of Sciences, the Ministerio de Ciencia, Innovación y Universidades, the National Aeronautics and Space Administration, the National Astronomical Observatory of Japan, the Nederlandse Onderzoekschool Voor Astronomie, the Norwegian Space Agency, the Research Council of Finland, the Romanian Space Agency, the Swiss Space Office (SSO) at the State Secretariat for Education, Research, and Innovation (SERI), and the United Kingdom Space Agency. A complete and detailed list is available on the *Euclid* web site (www.euclid-ec.org/consortium/community). This work has made use of CosmoHub, developed by PIC (maintained by IFAE and CIEMAT) in collaboration with ICE-CSIC. CosmoHub received funding from the Spanish government (MCIN/AEI/10.13039/501100011033), the EU NextGeneration/PRTR (PRTR-C17.II), and the Generalitat de Catalunya.

References

- Abbott, T. M. C., Abdalla, F. B., Alarcon, A., et al. 2018, PRD, 98, 043526
- Abbott, T. M. C., Aguena, M., Alarcon, A., et al. 2022, PRD, 105, 023520
- Aihara, H., Arimoto, N., Armstrong, R., et al. 2018, PASJ, 70, S4
- Albrecht, A., Bernstein, G., Cahn, R., et al. 2006, arXiv e-prints, arXiv:astro-ph/0609591
- Asgari, M., Lin, C.-A., Joachimi, B., et al. 2021, A&A, 645, A104
- Bakx, T., Kurita, T., Chisari, N. E., Vlah, Z., & Schmidt, F. 2023, JCAP, 10, 005
- Behroozi, P. S., Wechsler, R. H., & Wu, H.-Y. 2013, ApJ, 762, 109
- Blazek, J. A., MacCrann, N., Troxel, M. A., & Fang, X. 2019, PRD, 100, 103506
- Bridle, S. & King, L. 2007, NJP, 9, 444
- Brown, M. L., Taylor, A. N., Hambly, N. C., & Dye, S. 2002, MNRAS, 333, 501
- Camphuis, E., Benabed, K., Galli, S., Hivon, E., & Lilley, M. 2022, A&A, 668, A62
- Campos, A., Samuroff, S., & Mandelbaum, R. 2023, MNRAS, 525, 1885
- Carretero, J., Tallada, P., Casals, J., et al. 2017, in Proceedings of the European Physical Society Conference on High Energy Physics. 5-12 July, 488
- Catelan, P., Kamionkowski, M., & Blandford, R. D. 2001, MNRAS, 320, L7
- Cañas-Herrera, G., Bonici, M., Moretti, C., et al. 2025, cloe-org.github.io/v2025.10
- Challinor, A., Chon, G., Colombi, S., et al. 2011, PolSpice: Spatially Inhomogeneous Correlation Estimator for Temperature and Polarisation, Astrophysics Source Code Library, record ascl:1109.005
- Chen, S.-F. & Kokron, N. 2024, JCAP, 01, 027
- Chevallier, M. & Polarski, D. 2001, IJMPD, 10, 213
- Chisari, N. E. 2025, A&A Rev., 33, 5
- Chon, G., Challinor, A., Prunet, S., Hivon, E., & Szapudi, I. 2004, MNRAS, 350, 914
- Dark Energy Survey Collaboration: Abbott, T., Abdalla, F. B., Aleksic, J., et al. 2016, MNRAS, 460, 1270
- DeRose, J. & Chen, S.-F. 2025, arXiv e-prints, arXiv:2510.18981
- Deshpande, A. C., Kitching, T. D., Cardone, V. F., et al. 2020, A&A, 636, A95
- DESI Collaboration: Abareshi, B., Aguilar, J., Ahlen, S., et al. 2022, AJ, 164, 207
- Desjacques, V., Jeong, D., & Schmidt, F. 2018, Phys. Rep., 733, 1
- Di Matteo, T., Khandai, N., DeGraf, C., et al. 2012, ApJ, 745, L29
- Doux, C., Chang, C., Jain, B., et al. 2021, MNRAS, 503, 3796
- Doux, C., Jain, B., Zeurcher, D., et al. 2022, MNRAS, 515, 1942
- Dubois, Y., Pichon, C., Welker, C., et al. 2014, MNRAS, 444, 1453
- Euclid Collaboration: Blanchard, A., Camera, S., Carbone, C., et al. 2020, A&A, 642, A191
- Euclid Collaboration: Blot, L., Tanidis, K., Cañas-Herrera, G., et al. 2025, A&A, submitted, arXiv:2510.10021
- Euclid Collaboration: Cañas-Herrera, G., Goh, L. W. K., Blot, L., et al. 2025, A&A, submitted, arXiv:2510.09153
- Euclid Collaboration: Cardone, V. F., Joudaki, S., Blot, L., et al. 2025, A&A, submitted, arXiv:2510.09118
- Euclid Collaboration: Castander, F. J., Fosalba, P., Stadel, J., et al. 2025, A&A, 697, A5
- Euclid Collaboration: Goh, L. W. K., Nouri-Zonoz, A., Pamuk, S., et al. 2025, A&A, submitted, arXiv:2510.09147
- Euclid Collaboration: Hoffmann, K., Paviot, R., Joachimi, B., et al. 2026, arXiv e-prints, arXiv:2601.07785
- Euclid Collaboration: Knabenhans, M., Stadel, J., Potter, D., et al. 2021, MNRAS, 505, 2840
- Euclid Collaboration: Martinelli, M., Pezzotta, A., Sciotti, D., et al. 2025, A&A, submitted, arXiv:2510.09141
- Euclid Collaboration: Mathewson, W. L., Durrer, R., Camera, S., et al. 2025, A&A, submitted, arXiv:2510.17592
- Euclid Collaboration: Mellier, Y., Abdurro'uf, Acevedo Barroso, J. A., et al. 2025, A&A, 697, A1
- Euclid Collaboration: Paviot, R., Joachimi, B., Hoffmann, K., et al. 2026, arXiv e-prints, arXiv:2601.07784
- Euclid Collaboration: Tanidis, K., Cardone, V. F., Martinelli, M., et al. 2024, A&A, 683, A17
- Euclid Collaboration: Tessore, N., Joachimi, B., Loureiro, A., et al. 2025, A&A, 694, A141
- Euclid Collaboration: Tucci, M., Paltani, S., Hartley, W. G., et al. 2025, A&A, in press (Euclid Q1 SI), <https://doi.org/10.1051/0004-6361/202554588>, arXiv:2503.15306
- Fang, X., Blazek, J. A., McEwen, J. E., & Hirata, C. M. 2017, JCAP, 02, 030
- Feroz, F., Hobson, M. P., Cameron, E., & Pettitt, A. N. 2019, OJAp, 2, 10
- Fischbacher, S., Kacprzak, T., Blazek, J., & Refregier, A. 2023, JCAP, 01, 033
- Fortuna, M. C., Hoekstra, H., Joachimi, B., et al. 2021, MNRAS, 501, 2983
- Giblin, B., Heymans, C., Asgari, M., et al. 2021, A&A, 645, A105
- Griffith, R. L., Cooper, M. C., Newman, J. A., et al. 2012, ApJS, 200, 9
- Hambly, N., Irwin, M., & MacGillivray, H. 2001, MNRAS, 326, 1295
- Heymans, C., Tröster, T., Asgari, M., et al. 2021, A&A, 646, A140
- Hildebrandt, H., Viola, M., Heymans, C., et al. 2017, MNRAS, 465, 1454
- Hirata, C. M., Mandelbaum, R., Ishak, M., et al. 2007, MNRAS, 381, 1197
- Hirata, C. M. & Seljak, U. 2004, PRD, 70, 063526
- Hoekstra, H. 2021, A&A, 656, A135
- Howlett, C., Lewis, A., Hall, A., & Challinor, A. 2012, JCAP, 04, 027
- Ivezic, Ž., Kahn, S. M., Tyson, J. A., et al. 2019, ApJ, 873, 111
- Kaiser, N. 1984, ApJ, 284, L9
- Kaiser, N. 1987, MNRAS, 227, 1
- Kaviraj, S., Laigle, C., Kimm, T., et al. 2017, MNRAS, 467, 4739
- Khandai, N., Di Matteo, T., Croft, R., et al. 2015, MNRAS, 450, 1349
- Kilbinger, M. 2015, Rep. Prog. Phys., 78, 086901
- Kitching, T. D., Paykari, P., Hoekstra, H., & Cropper, M. 2019, OJAp, 2, 5
- Krause, E., Fang, X., Pandey, S., et al. 2021, arXiv e-prints, arXiv:2105.13548
- Kuijken, K., Heymans, C., Dvornik, A., et al. 2019, A&A, 625, A2
- Laigle, C., McCracken, H. J., Ilbert, O., et al. 2016, ApJS, 224, 24
- Lange, J. U. 2023, MNRAS, 525, 3181
- Le Brun, A. M. C., McCarthy, I. G., Schaye, J., & Ponman, T. J. 2014, MNRAS, 441, 1270
- Leonard, C. D., Rau, M. M., & Mandelbaum, R. 2024, PRD, 109, 083528
- Lewis, A., Challinor, A., & Lasenby, A. 2000, ApJ, 538, 473
- Li, S.-S., Hoekstra, H., Kuijken, K., et al. 2023, A&A, 679, A133
- Li, S.-S., Kuijken, K., Hoekstra, H., et al. 2021, A&A, 646, A175
- Limber, D. N. 1953, ApJ, 117, 134
- Linder, E. V. 2003, PRL, 90, 091301
- Maion, F., Angulo, R. E., Bakx, T., et al. 2024, MNRAS, 531, 2684
- Mandelbaum, R. 2018, ARA&A, 56, 393
- McCarthy, I. G., Schaye, J., Bird, S., & Le Brun, A. M. C. 2017, MNRAS, 465, 2936
- McEwen, J. E., Fang, X., Hirata, C. M., & Blazek, J. A. 2016, JCAP, 09, 015
- Mead, A. J., Brieden, S., Tröster, T., & Heymans, C. 2021, MNRAS, 502, 1401
- Mill, C. M., Danielle, L. C., Rau, M. M., Uhlemann, C., & Joudaki, S. 2025, J. Cosmology Astropart. Phys., 2025, 037
- Miller, L., Heymans, C., Kitching, T. D., et al. 2013, MNRAS, 429, 2858
- Miller, L., Kitching, T. D., Heymans, C., Heavens, A. F., & van Waerbeke, L. 2007, MNRAS, 382, 315
- More, S., Sugiyama, S., Miyatake, H., et al. 2023, PRD, 108, 123520
- Paopiamsap, A., Porqueres, N., Alonso, D., Harnois-Deraps, J., & Leonard, C. D. 2024, OJAp, 7, 34
- Patrignani, C., Particle Data Group, Agashe, K., et al. 2016, CPC, 40, 100001
- Porredon, A., Crocce, M., Fosalba, P., et al. 2021, Phys. Rev. D, 103, 043503
- Pozzetti, L., Hirata, C. M., Geach, J. E., et al. 2016, A&A, 590, A3
- Samuroff, S., Blazek, J., Troxel, M. A., et al. 2019, MNRAS, 489, 5453
- Samuroff, S., Campos, A., Porredon, A., & Blazek, J. 2024, OJAp, 7, 40
- Samuroff, S., Mandelbaum, R., & Blazek, J. 2021, MNRAS, 508, 637
- Samuroff, S., Mandelbaum, R., Blazek, J., et al. 2023, MNRAS, 524, 2195
- Schaye, J., Kugel, R., Schaller, M., et al. 2023, MNRAS, 526, 4978

- Schneider, M., Bridle, S., & Kirk, D. 2010, in American Astronomical Society Meeting Abstracts, Vol. 215, American Astronomical Society Meeting Abstracts #215, 376.01
- Schneider, P., van Waerbeke, L., & Mellier, Y. 2002, A&A, 389, 729
- Skilling, J. 2004, AIP Conference Proceedings, 735, 395
- Spergel, D., Gehrels, N., Baltay, C., et al. 2015, arXiv e-prints, arXiv:1503.03757
- Takahashi, R., Sato, M., Nishimichi, T., Taruya, A., & Oguri, M. 2012, ApJ, 761, 152
- Tallada, P., Carretero, J., Casals, J., et al. 2020, Astronomy and Computing, 32, 100391
- Taylor, P. L., Kitching, T., Cardone, V. F., et al. 2021, OJAp, 4, 6
- Troxel, M. A., MacCrann, N., Zuntz, J., et al. 2018, PRD, 98, 043528
- Vlah, Z., Chisari, N. E., & Schmidt, F. 2020, JCAP, 01, 025
- Vlah, Z., Chisari, N. E., & Schmidt, F. 2021, JCAP, 05, 061
- Wright, A. H., Hildebrandt, H., van den Busch, J. L., et al. 2025a, A&A, 703, A144
- Wright, A. H., Stölzner, B., Asgari, M., et al. 2025b, A&A, 703, A158
- Zuntz, J., Paterno, M., Jennings, E., et al. 2015, A&C, 12, 45

- ¹ Leiden Observatory, Leiden University, Einsteinweg 55, 2333 CC Leiden, The Netherlands
- ² Institute of Space Sciences (ICE, CSIC), Campus UAB, Carrer de Can Magrans, s/n, 08193 Barcelona, Spain
- ³ Institut d'Estudis Espacials de Catalunya (IEEC), Edifici RDIT, Campus UPC, 08860 Castelldefels, Barcelona, Spain
- ⁴ Institut de Recherche en Astrophysique et Planétologie (IRAP), Université de Toulouse, CNRS, UPS, CNES, 14 Av. Edouard Belin, 31400 Toulouse, France
- ⁵ Université Paris-Saclay, Université Paris Cité, CEA, CNRS, AIM, 91191, Gif-sur-Yvette, France
- ⁶ Department of Physics and Astronomy, University College London, Gower Street, London WC1E 6BT, UK
- ⁷ INAF-Osservatorio Astronomico di Roma, Via Frascati 33, 00078 Monteporzio Catone, Italy
- ⁸ INFN-Sezione di Roma, Piazzale Aldo Moro, 2 - c/o Dipartimento di Fisica, Edificio G. Marconi, 00185 Roma, Italy
- ⁹ Mullard Space Science Laboratory, University College London, Holmbury St Mary, Dorking, Surrey RH5 6NT, UK
- ¹⁰ Institute for Astronomy, University of Edinburgh, Royal Observatory, Blackford Hill, Edinburgh EH9 3HJ, UK
- ¹¹ Department of Physics, Astronomy and Mathematics, University of Hertfordshire, College Lane, Hatfield AL10 9AB, UK
- ¹² Centro de Investigaciones Energéticas, Medioambientales y Tecnológicas (CIEMAT), Avenida Complutense 40, 28040 Madrid, Spain
- ¹³ ESAC/ESA, Camino Bajo del Castillo, s/n., Urb. Villafranca del Castillo, 28692 Villanueva de la Cañada, Madrid, Spain
- ¹⁴ INAF-Osservatorio Astronomico di Brera, Via Brera 28, 20122 Milano, Italy
- ¹⁵ IFPU, Institute for Fundamental Physics of the Universe, via Beirut 2, 34151 Trieste, Italy
- ¹⁶ INAF-Osservatorio Astronomico di Trieste, Via G. B. Tiepolo 11, 34143 Trieste, Italy
- ¹⁷ INFN, Sezione di Trieste, Via Valerio 2, 34127 Trieste TS, Italy
- ¹⁸ SISSA, International School for Advanced Studies, Via Bonomea 265, 34136 Trieste TS, Italy
- ¹⁹ Dipartimento di Fisica e Astronomia, Università di Bologna, Via Gobetti 93/2, 40129 Bologna, Italy
- ²⁰ INAF-Osservatorio di Astrofisica e Scienza dello Spazio di Bologna, Via Piero Gobetti 93/3, 40129 Bologna, Italy
- ²¹ INFN-Sezione di Bologna, Viale Berti Pichat 6/2, 40127 Bologna, Italy
- ²² Dipartimento di Fisica, Università di Genova, Via Dodecaneso 33, 16146, Genova, Italy
- ²³ INFN-Sezione di Genova, Via Dodecaneso 33, 16146, Genova, Italy
- ²⁴ Department of Physics "E. Pancini", University Federico II, Via Cinthia 6, 80126, Napoli, Italy
- ²⁵ INAF-Osservatorio Astronomico di Capodimonte, Via Moiariello 16, 80131 Napoli, Italy
- ²⁶ Dipartimento di Fisica, Università degli Studi di Torino, Via P. Giuria 1, 10125 Torino, Italy
- ²⁷ INFN-Sezione di Torino, Via P. Giuria 1, 10125 Torino, Italy
- ²⁸ INAF-Osservatorio Astrofisico di Torino, Via Osservatorio 20, 10025 Pino Torinese (TO), Italy
- ²⁹ INAF-IASF Milano, Via Alfonso Corti 12, 20133 Milano, Italy
- ³⁰ Port d'Informació Científica, Campus UAB, C. Albareda s/n, 08193 Bellaterra (Barcelona), Spain
- ³¹ INFN section of Naples, Via Cinthia 6, 80126, Napoli, Italy
- ³² Institute for Astronomy, University of Hawaii, 2680 Woodlawn Drive, Honolulu, HI 96822, USA
- ³³ Instituto de Astrofísica de Canarias, E-38205 La Laguna, Tenerife, Spain
- ³⁴ Jodrell Bank Centre for Astrophysics, Department of Physics and Astronomy, University of Manchester, Oxford Road, Manchester M13 9PL, UK
- ³⁵ European Space Agency/ESRIN, Largo Galileo Galilei 1, 00044 Frascati, Roma, Italy
- ³⁶ Université Claude Bernard Lyon 1, CNRS/IN2P3, IP2I Lyon, UMR 5822, Villeurbanne, F-69100, France
- ³⁷ Institut de Ciències del Cosmos (ICCUB), Universitat de Barcelona (IEEC-UB), Martí i Franquès 1, 08028 Barcelona, Spain
- ³⁸ Institució Catalana de Recerca i Estudis Avançats (ICREA), Passeig de Lluís Companys 23, 08010 Barcelona, Spain
- ³⁹ Institut de Ciències de l'Espai (IEEC-CSIC), Campus UAB, Carrer de Can Magrans, s/n Cerdanyola del Vallés, 08193 Barcelona, Spain
- ⁴⁰ UCB Lyon 1, CNRS/IN2P3, IUF, IP2I Lyon, 4 rue Enrico Fermi, 69622 Villeurbanne, France
- ⁴¹ Departamento de Física, Faculdade de Ciências, Universidade de Lisboa, Edifício C8, Campo Grande, PT1749-016 Lisboa, Portugal
- ⁴² Instituto de Astrofísica e Ciências do Espaço, Faculdade de Ciências, Universidade de Lisboa, Campo Grande, 1749-016 Lisboa, Portugal
- ⁴³ Department of Astronomy, University of Geneva, ch. d'Ecogia 16, 1290 Versoix, Switzerland
- ⁴⁴ Université Paris-Saclay, CNRS, Institut d'astrophysique spatiale, 91405, Orsay, France
- ⁴⁵ Aix-Marseille Université, CNRS/IN2P3, CPPM, Marseille, France
- ⁴⁶ INAF-Istituto di Astrofisica e Planetologia Spaziali, via del Fosso del Cavaliere, 100, 00100 Roma, Italy
- ⁴⁷ INFN-Bologna, Via Irnerio 46, 40126 Bologna, Italy
- ⁴⁸ School of Physics, HH Wills Physics Laboratory, University of Bristol, Tyndall Avenue, Bristol, BS8 1TL, UK
- ⁴⁹ University Observatory, LMU Faculty of Physics, Scheinerstr. 1, 81679 Munich, Germany
- ⁵⁰ Max Planck Institute for Extraterrestrial Physics, Giessenbachstr. 1, 85748 Garching, Germany
- ⁵¹ INAF-Osservatorio Astronomico di Padova, Via dell'Osservatorio 5, 35122 Padova, Italy
- ⁵² Universitäts-Sternwarte München, Fakultät für Physik, Ludwig-Maximilians-Universität München, Scheinerstr. 1, 81679 München, Germany
- ⁵³ Institute of Theoretical Astrophysics, University of Oslo, P.O. Box 1029 Blindern, 0315 Oslo, Norway
- ⁵⁴ Jet Propulsion Laboratory, California Institute of Technology, 4800 Oak Grove Drive, Pasadena, CA, 91109, USA
- ⁵⁵ Felix Hormuth Engineering, Goethestr. 17, 69181 Leimen, Germany
- ⁵⁶ Technical University of Denmark, Elektrovej 327, 2800 Kgs. Lyngby, Denmark
- ⁵⁷ Cosmic Dawn Center (DAWN), Denmark
- ⁵⁸ Max-Planck-Institut für Astronomie, Königstuhl 17, 69117 Heidelberg, Germany
- ⁵⁹ Université de Genève, Département de Physique Théorique and Centre for Astroparticle Physics, 24 quai Ernest-Ansermet, CH-1211 Genève 4, Switzerland
- ⁶⁰ Department of Physics, P.O. Box 64, University of Helsinki, 00014 Helsinki, Finland

- ⁶¹ Helsinki Institute of Physics, Gustaf Hällströmin katu 2, University of Helsinki, 00014 Helsinki, Finland
- ⁶² Laboratoire d'étude de l'Univers et des phénomènes eXtremes, Observatoire de Paris, Université PSL, Sorbonne Université, CNRS, 92190 Meudon, France
- ⁶³ SKAO, Jodrell Bank, Lower Withington, Macclesfield SK11 9FT, UK
- ⁶⁴ Centre de Calcul de l'IN2P3/CNRS, 21 avenue Pierre de Coubertin 69627 Villeurbanne Cedex, France
- ⁶⁵ Universität Bonn, Argelander-Institut für Astronomie, Auf dem Hügel 71, 53121 Bonn, Germany
- ⁶⁶ Aix-Marseille Université, CNRS, CNES, LAM, Marseille, France
- ⁶⁷ Dipartimento di Fisica e Astronomia "Augusto Righi" - Alma Mater Studiorum Università di Bologna, via Piero Gobetti 93/2, 40129 Bologna, Italy
- ⁶⁸ Institute of Physics, Laboratory of Astrophysics, Ecole Polytechnique Fédérale de Lausanne (EPFL), Observatoire de Sauverny, 1290 Versoix, Switzerland
- ⁶⁹ Telespazio UK S.L. for European Space Agency (ESA), Camino bajo del Castillo, s/n, Urbanizacion Villafranca del Castillo, Villanueva de la Cañada, 28692 Madrid, Spain
- ⁷⁰ Institut de Física d'Altes Energies (IFAE), The Barcelona Institute of Science and Technology, Campus UAB, 08193 Bellaterra (Barcelona), Spain
- ⁷¹ European Space Agency/ESTEC, Keplerlaan 1, 2201 AZ Noordwijk, The Netherlands
- ⁷² DARK, Niels Bohr Institute, University of Copenhagen, Jagtvej 155, 2200 Copenhagen, Denmark
- ⁷³ Waterloo Centre for Astrophysics, University of Waterloo, Waterloo, Ontario N2L 3G1, Canada
- ⁷⁴ Department of Physics and Astronomy, University of Waterloo, Waterloo, Ontario N2L 3G1, Canada
- ⁷⁵ Perimeter Institute for Theoretical Physics, Waterloo, Ontario N2L 2Y5, Canada
- ⁷⁶ Space Science Data Center, Italian Space Agency, via del Politecnico snc, 00133 Roma, Italy
- ⁷⁷ Centre National d'Etudes Spatiales – Centre spatial de Toulouse, 18 avenue Edouard Belin, 31401 Toulouse Cedex 9, France
- ⁷⁸ Institute of Space Science, Str. Atomistilor, nr. 409 Măgurele, Ilfov, 077125, Romania
- ⁷⁹ Dipartimento di Fisica e Astronomia "G. Galilei", Università di Padova, Via Marzolo 8, 35131 Padova, Italy
- ⁸⁰ INFN-Padova, Via Marzolo 8, 35131 Padova, Italy
- ⁸¹ Université Paris Cité, CNRS, Astroparticule et Cosmologie, 75013 Paris, France
- ⁸² Instituto de Física Teórica UAM-CSIC, Campus de Cantoblanco, 28049 Madrid, Spain
- ⁸³ Université St Joseph; Faculty of Sciences, Beirut, Lebanon
- ⁸⁴ Departamento de Física, FCFM, Universidad de Chile, Blanco Encalada 2008, Santiago, Chile
- ⁸⁵ Universität Innsbruck, Institut für Astro- und Teilchenphysik, Technikerstr. 25/8, 6020 Innsbruck, Austria
- ⁸⁶ Department of Physics and Helsinki Institute of Physics, Gustaf Hällströmin katu 2, University of Helsinki, 00014 Helsinki, Finland
- ⁸⁷ Department of Physics, Royal Holloway, University of London, Surrey TW20 0EX, UK
- ⁸⁸ Instituto de Astrofísica e Ciências do Espaço, Faculdade de Ciências, Universidade de Lisboa, Tapada da Ajuda, 1349-018 Lisboa, Portugal
- ⁸⁹ Cosmic Dawn Center (DAWN)
- ⁹⁰ Niels Bohr Institute, University of Copenhagen, Jagtvej 128, 2200 Copenhagen, Denmark
- ⁹¹ Universidad Politécnica de Cartagena, Departamento de Electrónica y Tecnología de Computadoras, Plaza del Hospital 1, 30202 Cartagena, Spain
- ⁹² Kapteyn Astronomical Institute, University of Groningen, PO Box 800, 9700 AV Groningen, The Netherlands
- ⁹³ Caltech/IPAC, 1200 E. California Blvd., Pasadena, CA 91125, USA
- ⁹⁴ Dipartimento di Fisica e Scienze della Terra, Università degli Studi di Ferrara, Via Giuseppe Saragat 1, 44122 Ferrara, Italy
- ⁹⁵ Istituto Nazionale di Fisica Nucleare, Sezione di Ferrara, Via Giuseppe Saragat 1, 44122 Ferrara, Italy
- ⁹⁶ INAF, Istituto di Radioastronomia, Via Piero Gobetti 101, 40129 Bologna, Italy
- ⁹⁷ Astronomical Observatory of the Autonomous Region of the Aosta Valley (OAVdA), Loc. Lignan 39, I-11020, Nus (Aosta Valley), Italy
- ⁹⁸ Université Côte d'Azur, Observatoire de la Côte d'Azur, CNRS, Laboratoire Lagrange, Bd de l'Observatoire, CS 34229, 06304 Nice cedex 4, France
- ⁹⁹ ICSC - Centro Nazionale di Ricerca in High Performance Computing, Big Data e Quantum Computing, Via Magnanelli 2, Bologna, Italy
- ¹⁰⁰ Department of Physics, Oxford University, Keble Road, Oxford OX1 3RH, UK
- ¹⁰¹ Univ. Grenoble Alpes, CNRS, Grenoble INP, LPSC-IN2P3, 53, Avenue des Martyrs, 38000, Grenoble, France
- ¹⁰² Dipartimento di Fisica, Sapienza Università di Roma, Piazzale Aldo Moro 2, 00185 Roma, Italy
- ¹⁰³ Aurora Technology for European Space Agency (ESA), Camino bajo del Castillo, s/n, Urbanizacion Villafranca del Castillo, Villanueva de la Cañada, 28692 Madrid, Spain
- ¹⁰⁴ Dipartimento di Fisica e Astronomia "Augusto Righi" - Alma Mater Studiorum Università di Bologna, Viale Berti Pichat 6/2, 40127 Bologna, Italy
- ¹⁰⁵ Dipartimento di Fisica - Sezione di Astronomia, Università di Trieste, Via Tiepolo 11, 34131 Trieste, Italy
- ¹⁰⁶ Institut d'Astrophysique de Paris, 98bis Boulevard Arago, 75014, Paris, France
- ¹⁰⁷ ICL, Junia, Université Catholique de Lille, LITL, 59000 Lille, France
- ¹⁰⁸ CERCA/ISO, Department of Physics, Case Western Reserve University, 10900 Euclid Avenue, Cleveland, OH 44106, USA
- ¹⁰⁹ Laboratoire Univers et Théorie, Observatoire de Paris, Université PSL, Université Paris Cité, CNRS, 92190 Meudon, France
- ¹¹⁰ Dipartimento di Fisica "Aldo Pontremoli", Università degli Studi di Milano, Via Celoria 16, 20133 Milano, Italy
- ¹¹¹ INFN-Sezione di Milano, Via Celoria 16, 20133 Milano, Italy
- ¹¹² Departamento de Física Fundamental, Universidad de Salamanca, Plaza de la Merced s/n, 37008 Salamanca, Spain
- ¹¹³ Aix-Marseille Université, Université de Toulon, CNRS, CPT, Marseille, France
- ¹¹⁴ Université de Strasbourg, CNRS, Observatoire astronomique de Strasbourg, UMR 7550, 67000 Strasbourg, France
- ¹¹⁵ Center for Data-Driven Discovery, Kavli IPMU (WPI), UTIAS, The University of Tokyo, Kashiwa, Chiba 277-8583, Japan
- ¹¹⁶ California Institute of Technology, 1200 E California Blvd, Pasadena, CA 91125, USA
- ¹¹⁷ Department of Mathematics and Physics E. De Giorgi, University of Salento, Via per Arnesano, CP-193, 73100, Lecce, Italy
- ¹¹⁸ INFN, Sezione di Lecce, Via per Arnesano, CP-193, 73100, Lecce, Italy
- ¹¹⁹ INAF-Sezione di Lecce, c/o Dipartimento Matematica e Fisica, Via per Arnesano, 73100, Lecce, Italy
- ¹²⁰ Departamento Física Aplicada, Universidad Politécnica de Cartagena, Campus Muralla del Mar, 30202 Cartagena, Murcia, Spain
- ¹²¹ Instituto de Física de Cantabria, Edificio Juan Jordá, Avenida de los Castros, 39005 Santander, Spain
- ¹²² Observatorio Nacional, Rua General Jose Cristina, 77-Bairro Imperial de São Cristóvão, Rio de Janeiro, 20921-400, Brazil
- ¹²³ Institute of Cosmology and Gravitation, University of Portsmouth, Portsmouth PO1 3FX, UK
- ¹²⁴ Departament de Física, Universitat Autònoma de Barcelona, 08193 Bellaterra (Barcelona), Spain
- ¹²⁵ Instituto de Astronomía Teórica y Experimental (IATE-CONICET), Laprida 854, X5000BGR, Córdoba, Argentina
- ¹²⁶ Department of Computer Science, Aalto University, PO Box 15400, Espoo, FI-00 076, Finland

- ¹²⁷ Universidad de La Laguna, Dpto. Astrofísica, E-38206 La Laguna, Tenerife, Spain
- ¹²⁸ Ruhr University Bochum, Faculty of Physics and Astronomy, Astronomical Institute (AIRUB), German Centre for Cosmological Lensing (GCCL), 44780 Bochum, Germany
- ¹²⁹ Department of Physics and Astronomy, Vesilinnantie 5, University of Turku, 20014 Turku, Finland
- ¹³⁰ Finnish Centre for Astronomy with ESO (FINCA), Quantum, Vesilinnantie 5, University of Turku, 20014 Turku, Finland
- ¹³¹ Serco for European Space Agency (ESA), Camino bajo del Castillo, s/n, Urbanizacion Villafranca del Castillo, Villanueva de la Cañada, 28692 Madrid, Spain
- ¹³² ARC Centre of Excellence for Dark Matter Particle Physics, Melbourne, Australia
- ¹³³ Centre for Astrophysics & Supercomputing, Swinburne University of Technology, Hawthorn, Victoria 3122, Australia
- ¹³⁴ Department of Physics and Astronomy, University of the Western Cape, Bellville, Cape Town, 7535, South Africa
- ¹³⁵ DAMTP, Centre for Mathematical Sciences, Wilberforce Road, Cambridge CB3 0WA, UK
- ¹³⁶ Kavli Institute for Cosmology Cambridge, Madingley Road, Cambridge, CB3 0HA, UK
- ¹³⁷ Institut d'Astrophysique de Paris, UMR 7095, CNRS, and Sorbonne Université, 98 bis boulevard Arago, 75014 Paris, France
- ¹³⁸ Department of Theoretical Physics, University of Geneva, Switzerland
- ¹³⁹ Department of Physics, Centre for Extragalactic Astronomy, Durham University, South Road, Durham, DH1 3LE, UK
- ¹⁴⁰ Department of Physics, Institute for Computational Cosmology, Durham University, South Road, Durham, DH1 3LE, UK
- ¹⁴¹ Institute for Theoretical Particle Physics and Cosmology (TTK), RWTH Aachen University, 52056 Aachen, Germany
- ¹⁴² IRFU, CEA, Université Paris-Saclay 91191 Gif-sur-Yvette Cedex, France
- ¹⁴³ INAF-Osservatorio Astrofisico di Arcetri, Largo E. Fermi 5, 50125, Firenze, Italy
- ¹⁴⁴ Centro de Astrofísica da Universidade do Porto, Rua das Estrelas, 4150-762 Porto, Portugal
- ¹⁴⁵ Instituto de Astrofísica e Ciências do Espaço, Universidade do Porto, CAUP, Rua das Estrelas, PT4150-762 Porto, Portugal
- ¹⁴⁶ HE Space for European Space Agency (ESA), Camino bajo del Castillo, s/n, Urbanizacion Villafranca del Castillo, Villanueva de la Cañada, 28692 Madrid, Spain
- ¹⁴⁷ Department of Astrophysics, University of Zurich, Winterthurerstrasse 190, 8057 Zurich, Switzerland
- ¹⁴⁸ University of Applied Sciences and Arts of Northwestern Switzerland, School of Computer Science, 5210 Windisch, Switzerland
- ¹⁴⁹ INAF - Osservatorio Astronomico d'Abruzzo, Via Maggini, 64100, Teramo, Italy
- ¹⁵⁰ Theoretical astrophysics, Department of Physics and Astronomy, Uppsala University, Box 516, 751 37 Uppsala, Sweden
- ¹⁵¹ Mathematical Institute, University of Leiden, Einsteinweg 55, 2333 CA Leiden, The Netherlands
- ¹⁵² Institute of Astronomy, University of Cambridge, Madingley Road, Cambridge CB3 0HA, UK
- ¹⁵³ Center for Astrophysics and Cosmology, University of Nova Gorica, Nova Gorica, Slovenia
- ¹⁵⁴ Institute for Particle Physics and Astrophysics, Dept. of Physics, ETH Zurich, Wolfgang-Pauli-Strasse 27, 8093 Zurich, Switzerland
- ¹⁵⁵ Department of Astrophysical Sciences, Peyton Hall, Princeton University, Princeton, NJ 08544, USA
- ¹⁵⁶ Institut de Physique Théorique, CEA, CNRS, Université Paris-Saclay 91191 Gif-sur-Yvette Cedex, France
- ¹⁵⁷ International Centre for Theoretical Physics (ICTP), Strada Costiera 11, 34151 Trieste, Italy
- ¹⁵⁸ Center for Computational Astrophysics, Flatiron Institute, 162 5th Avenue, 10010, New York, NY, USA
- ¹⁵⁹ Kavli Institute for Particle Astrophysics & Cosmology (KIPAC), Stanford University, Stanford, CA 94305, USA
- ¹⁶⁰ SLAC National Accelerator Laboratory, 2575 Sand Hill Road, Menlo Park, CA 94025, USA

Appendix A: Comparison of Flagship C_ℓ with theoretical descriptions from CosmoSIS

Here, we show how the measured C_ℓ in Flagship (Sect. 4.3) compare to the z NLA and z TATT theoretical predictions, based on the constrained values from Fig. 3. Figure A.1 shows this comparison for the case of the WL C_ℓ for all the $i-j$ combinations of source tomographic redshift bins. For each panel, in the upper plot we include the measured Flagship C_ℓ (black points), the z TATT (tan shaded area), and the z NLA (blue shaded area) predictions, where the uncertainties from the theoretical predictions assume a Gaussian covariance for the *Euclid* DR1 setup (Sect. 4.2). In this case, we do not compute the super-sample and the connected non-Gaussian covariance terms because they are subdominant and are not expected to strongly affect the recovered IA values. The bottom panels show the differences between the measured Flagship C_ℓ and the theoretical predictions divided by the uncertainty, where the tan and blue lines correspond to the z TATT and z NLA cases, respectively. The black and grey shaded horizontal lines in the bottom plots show the 1σ and 2σ limits. The dotted black vertical lines show the scale cuts that were used to constrain the IA parameters in Fig. 3, corresponding to $k_{\max} = 3 h \text{ Mpc}^{-1}$. Both z NLA and z TATT are able to describe the WL C_ℓ measured in Flagship, generally with maximum differences of 2σ . However, z TATT allows us to better describe the Flagship DV, especially when cross-correlating low and high redshift bins. Figure A.2 shows the comparison for the case of the GGL C_ℓ , where both z NLA and z TATT theory predictions are able to describe the measured C_ℓ , up to the corresponding scale cuts, with a similar level of accuracy. Finally, Fig. A.3 shows the comparison of the GC C_ℓ for the auto-correlation of lens redshift bins, in general showing a good agreement. However, the high-redshift bin shows some discrepancy at large scales, which potentially originates from the evolution of the galaxy bias parameter in the redshift range covered by this wide bin (see Fig. 2). As explained in Sect. 3.2, the galaxy bias parameters are obtained by fitting the angular correlation functions to the samples of this analysis. However, if the galaxy bias evolves within the redshift bin, the estimated galaxy bias will only be an approximation, which can lead to the differences we observe in Fig. A.3. Nevertheless, this is not an issue for our study, since we are able to accurately describe the Flagship WL and GGL C_ℓ , which encode the IA information, and the galaxy bias values we employ for our fiducial analyses are used for synthetic DVs.

Appendix B: IA values derived from Euclid Collaboration: Paviot et al.'s paper

To assess a robust estimation of the IA values in this work, we compare the IA constraints obtained following our methodology with those from P26, which also used the Flagship simulation for their analysis on the IA evolution with galaxy properties. However, there are some differences between the two analyses, both in terms of IA estimators and in the galaxy sample definition, that need to be understood before performing this comparison. Regarding the IA estimators, this work derives the IA values by fitting WL, GGL, and GC C_ℓ , where we define a source and a lens catalogue; while P26 employ the so-called w_{gg} , w_{g+} , and w_{++} correlation functions, which are commonly used in IA studies. These correlation functions define density and shape samples, which trace the galaxy positions and the shapes of the galaxies, respectively. Moreover, they only correlate objects that are close to each other, in terms of angular and radial distance. In this way, they do not cross-correlate samples at different red-

shift bins, as in the case of our study. For the galaxy sample definition, we do not apply a direct magnitude cut in our source sample (which is the one mainly driving IA), while P26 perform an apparent magnitude cut, such that $I_E < 24.5$. Besides that, P26 generate ten redshift bins of size $\Delta z = 0.2$ between $0.1 < z < 2.1$, and subsample the catalogue down to a number density of $1.5 \text{ galaxies/arcmin}^2$ to reduce computation time. Instead, we perform a cut in the photo- z range of $0.2 < z_b < 2.5$, and generate six equipopulated tomographic bins for sources and for lenses, where the number density of sources is $\sim 5.99 \text{ galaxies/arcmin}^2$. Finally, the scale cuts employed by both analyses are applied in a different space. P26 define scale cuts based on configuration space, such that $r_p > 5 h^{-1} \text{ Mpc}$ (with r_p the transverse distance between objects), while this work applies cuts in harmonic space, leading to $k_{\max} < 3 h \text{ Mpc}^{-1}$ for WL C_ℓ , and $k_{\max} < 0.3 h \text{ Mpc}^{-1}$ for GGL and GC C_ℓ .

All these reasons make it unfeasible to directly compare the constraints we obtained in Fig. 3 with those obtained in P26. Thus, we modify our sample definition to more closely resemble that of P26. In particular, we generate a new source catalogue by applying the same magnitude cut as in P26 ($I_E < 24.5$). We also test the effect of removing the last source and lens redshift bins, since P26 are unable to fit the IA parameters properly at $z > 1.1$. This could be related to the fact that the IA implementation in Flagship is not accurate enough at high redshifts, considering the lack of IA observations in this regime, and the fact that Flagship was calibrated at $z = 1$ with the hydro-dynamical simulation Horizon-AGN (Dubois et al. 2014; Kaviraj et al. 2017) and extrapolated to higher redshifts (Euclid Collaboration: Hoffmann et al. 2026). Figure B.1 shows the z TATT constraints derived by P26 (black unfilled contours), together with the constraints derived in this analysis by applying an $I_E < 24.5$ magnitude cut (tan contours) and by also removing the last source and lens tomographic redshift bin (blue contours). For each case, we include the χ^2_v . We can see that, in general, the posterior distributions of the z TATT parameters from P26 overlap with ours with tensions below 2σ , with the largest differences in the η_1 and $A_{1\delta}$ parameters. We also note that removing the last redshift bins increases the overlap with P26, especially for the A_2 and η_1 parameters. As in the case of P26, we find a large χ^2_v when including the last redshift bins, which is much reduced when removing them. Although there are still some differences between both studies, which come from the different analysis choices described above, the level of overlap with the results from P26 allows us to confirm the robust measurement of IA values in this work.

Since we obtain a worse fit when including all the redshift bins in our modified sample selection (source catalogue with $I_E < 24.5$), we check if this also happens when using the fiducial sample selection defined in Sect. 4.2. Figure B.2 shows the z TATT constraints derived in the fiducial analysis when considering all the redshift bins (tan, same z TATT constraints as in Fig. 3) and when removing the last lens and source redshift bins (blue), together with their χ^2_v . As in the modified sample definition, we obtain a large χ^2_v when including all the redshift bins, while it behaves well if we remove the last ones. However, we note the large level of overlap in the z TATT constraints in both cases. This indicates that the IA fiducial values that were used to generate the synthetic DVs (Sect. 4) are valid, as it was also seen in Fig. 3 and Figs. A.1–A.3.

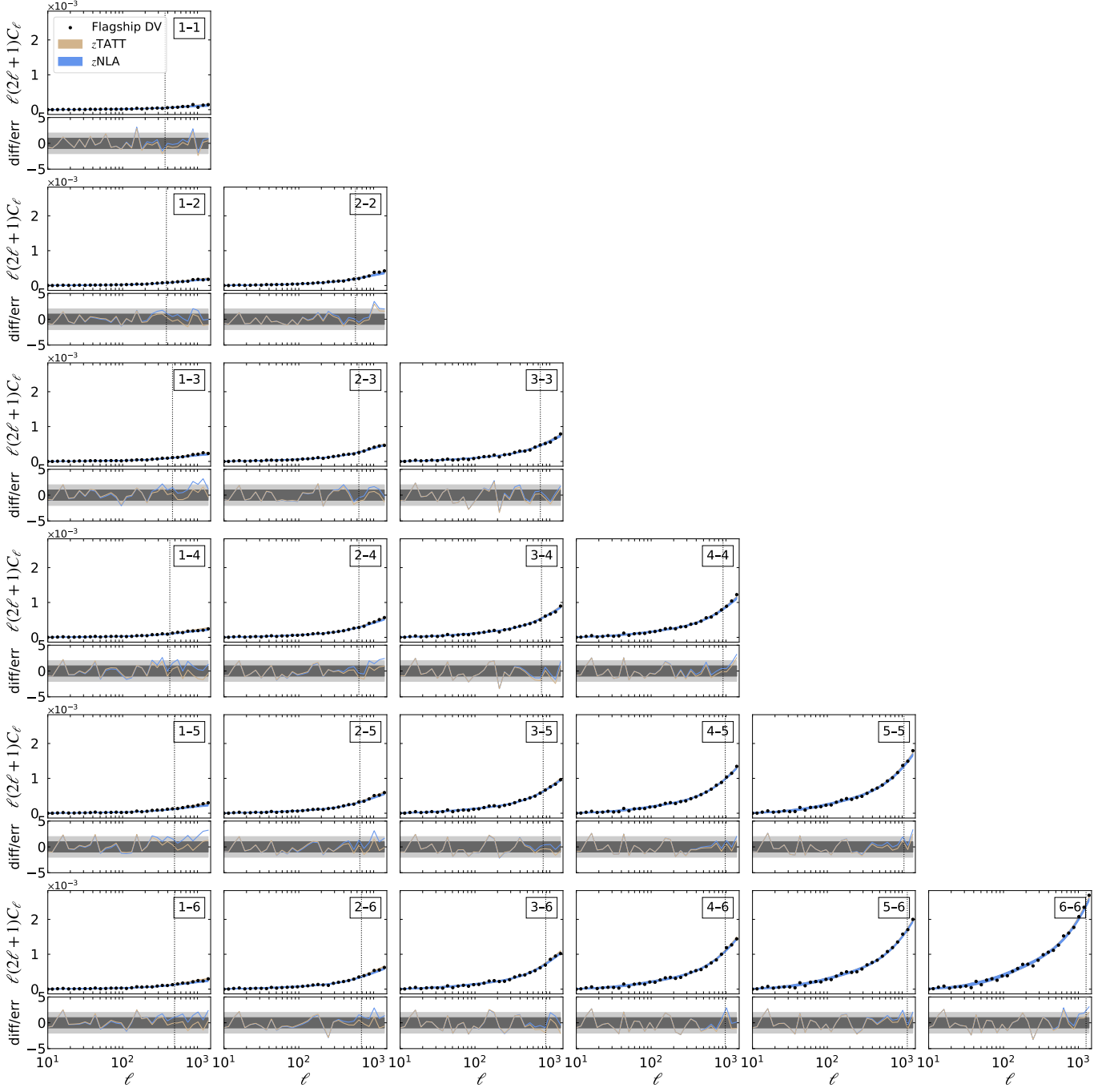


Fig. A.1. (Top): Comparison of the measured WL C_ℓ from Flagship (black) against z TATT (tan) and z NLA (blue) theoretical predictions for the different combinations of source tomographic redshift bins. Theoretical uncertainties assume a Gaussian covariance matrix with a DR1 area. Scale cuts are shown as dotted vertical lines. (Bottom): Ratio of the difference between the measured C_ℓ and the theoretical predictions over the uncertainty.

Appendix C: Constraining power with fixed nuisance parameters

Here, we study the constraining power when only sampling over the cosmological and IA parameters. In this way, we can assess whether the lack of difference in constraining power between z NLA and z TATT in Sect. 5.1 is preserved in a more optimal scenario, where all other nuisance parameters are fixed.

Figure C.1 shows the posterior distributions for the IA (left) and the cosmological (right) parameters when modelling the DV with z TATT (tan) or z NLA (blue) as a function of the scale cuts

applied to the WL C_ℓ : $k_{\max} = 1 \text{ h Mpc}^{-1}$ (dashed unfilled contours) and $k_{\max} = 3 \text{ h Mpc}^{-1}$ (filled contours). This is the same analysis performed in Fig. 4, but with the nuisance parameters fixed. Even though both IA and cosmological parameters are more constrained than in Fig. 4, as expected when reducing the parameter space by fixing the nuisance parameters to their fiducial values, the same conclusion as in Fig. 4 arises: z NLA and z TATT yield very similar constraining power on the cosmological parameters at $k_{\max} = 3 \text{ h Mpc}^{-1}$, while the z TATT higher-order terms are unconstrained at $k_{\max} = 1 \text{ h Mpc}^{-1}$. This indicates that we will not lose constraining power by choosing a

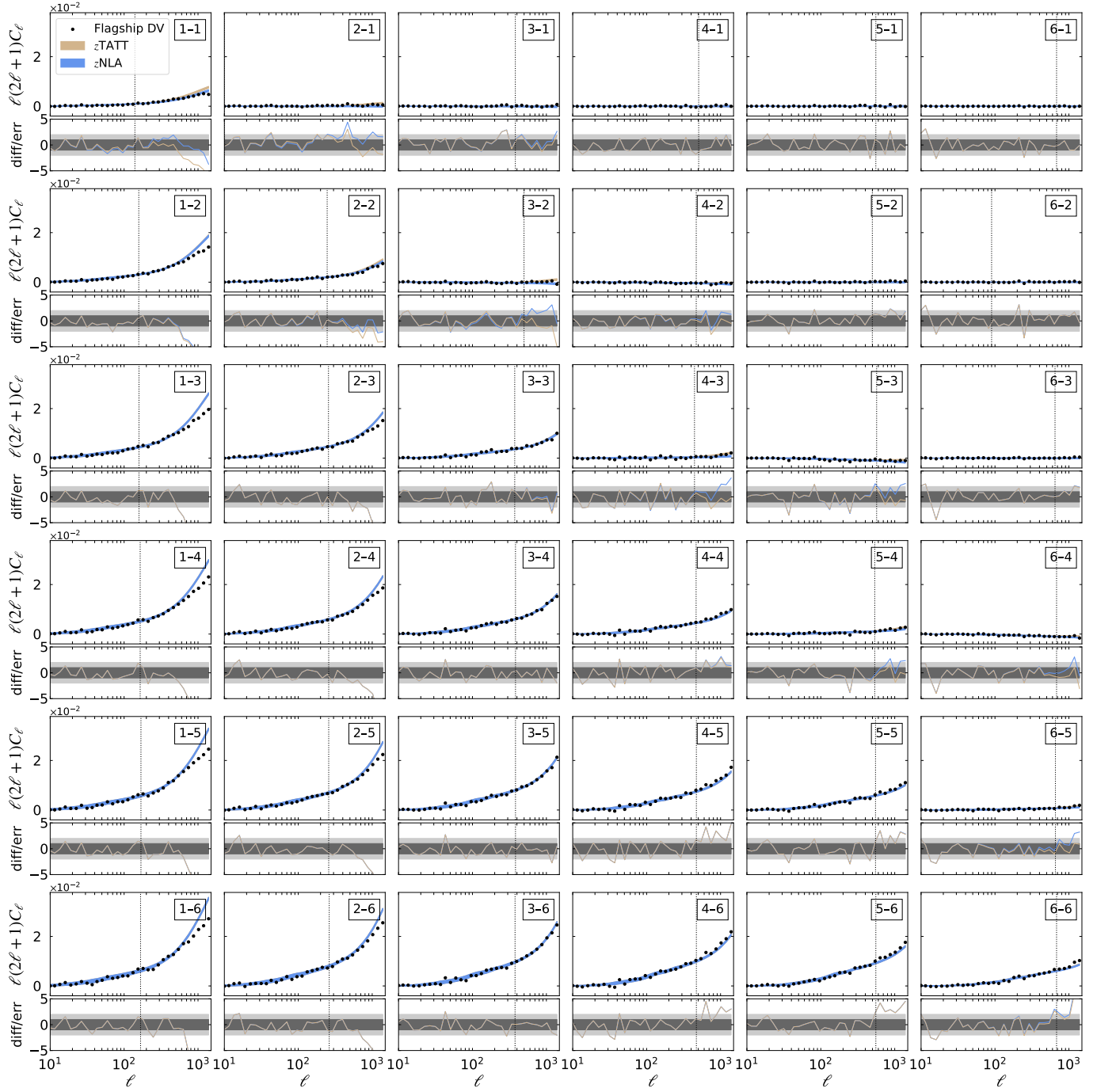


Fig. A.2. Same as Fig. A.1 but for the GGL C_ℓ from Flagship, where the $i-j$ tomographic redshift bin combinations correspond to the i lens and the j source bins.

more flexible model, such as z TATT, if we include scales small enough, even if we are able to reduce the uncertainties on the nuisance parameters with respect to our fiducial analysis, as defined in Table 3.

Figure C.2 shows the S_8 and Ω_m constraints for different combinations of cosmological probes (3×2 pt, 2×2 pt, and WL) for z TATT and z NLA. This is the same configuration as Fig. 6, where we saw that there is no difference in constraining power between z TATT and z NLA for the 2×2 pt and WL cases. This is also true when fixing all nuisance parameters (except from IA), as can be seen in Fig. C.2. However, in this case, we can see the typical degeneracy between S_8 and Ω_m in the WL-only case,

which was diluted in Fig. 6 by the lower constraining power of that scenario. The tight degeneracy between S_8 and Ω_m for 3×2 pt and 2×2 pt arises mainly from fixing the galaxy bias terms.

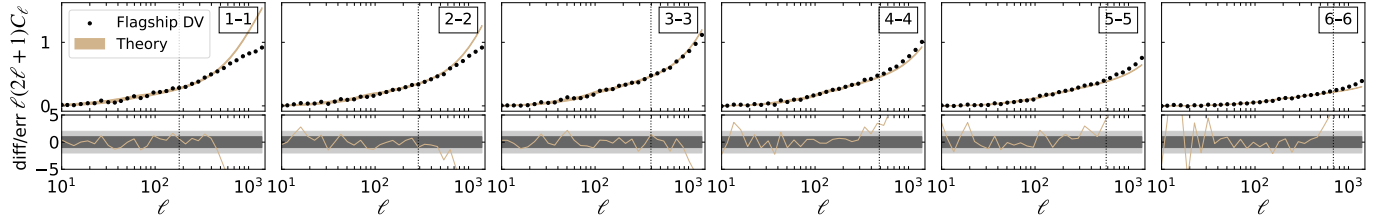


Fig. A.3. Same as Fig. A.1 but for the GC C_ℓ from Flagship, where we only include the auto-correlation of the lens bins.

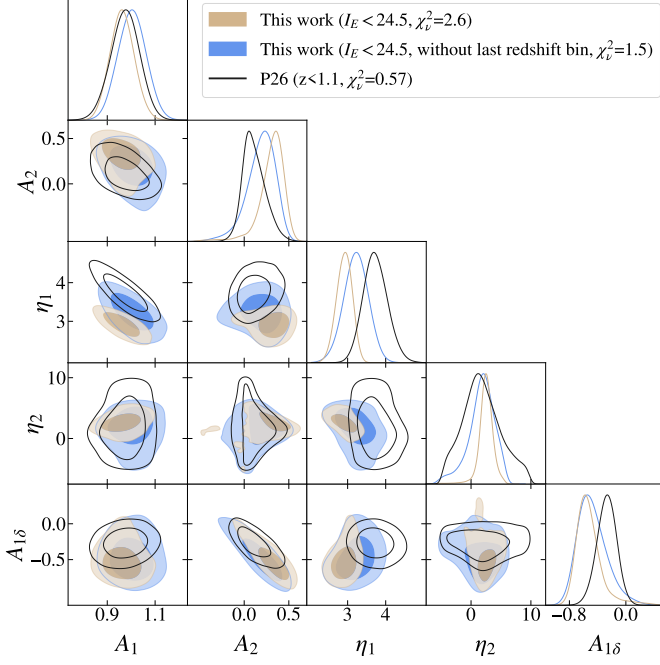


Fig. B.1. Comparison of the z TATT IA parameter constraints and the χ^2_ν estimates derived from Flagship for 3 cases: i) applying an apparent magnitude cut $I_E < 24.5$ to the source catalogue (tan), ii) applying the magnitude cut and removing the last lens and source redshift bin (blue), and iii) the constraints derived in P26 (black).

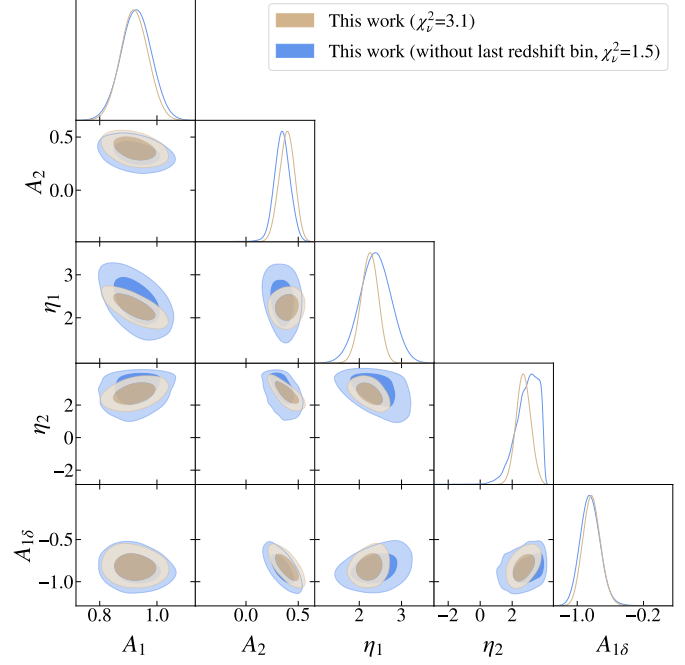


Fig. B.2. Comparison of the z TATT IA parameter constraints and the χ^2_ν estimates derived from Flagship for 2 cases: i) fiducial sample selection (tan, Sect. 4.2), and ii) removing the last lens and source redshift bin from the fiducial sample selection (blue).

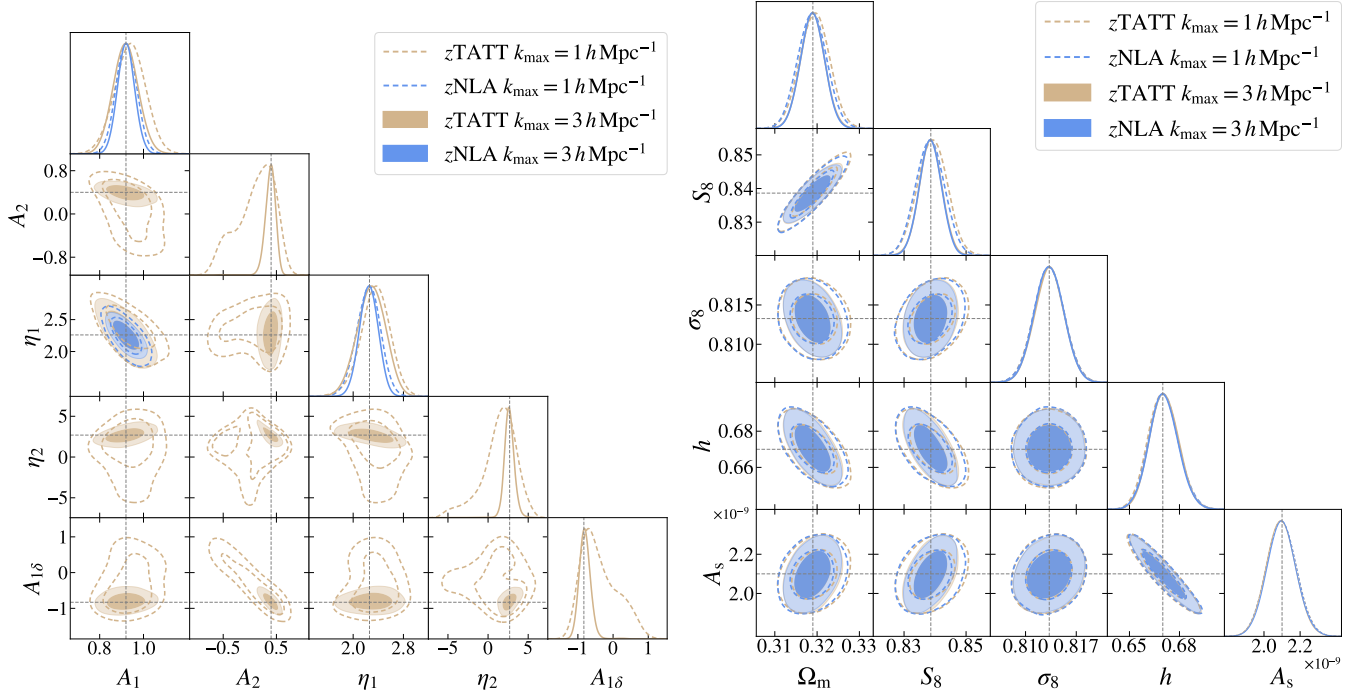


Fig. C.1. Same as Fig. 4, but only sampling over the IA and cosmological parameters. Hence, the nuisance parameters are fixed to their fiducial values. The tan contours on the right plot are not well distinguished because they overlap with the blue ones.

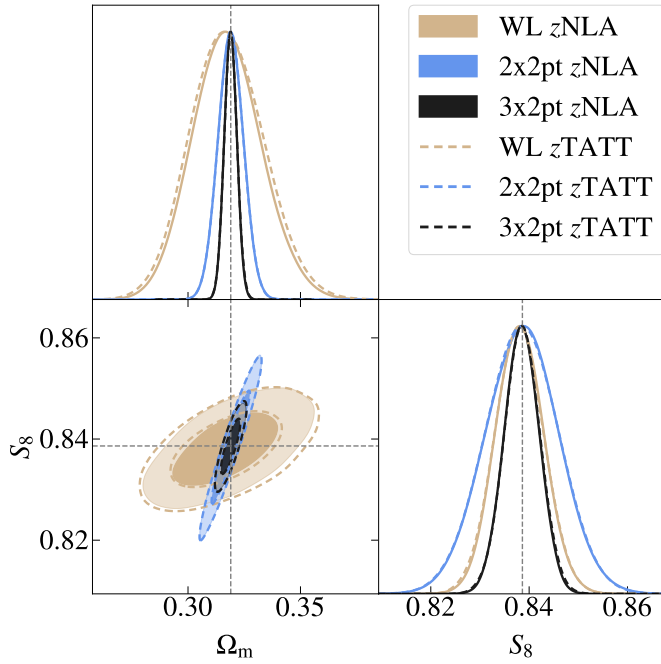


Fig. C.2. Same as Fig. 6, but only sampling over the IA and cosmological parameters. The nuisance parameters have been fixed to their fiducial values.